Adaptable internal representations drive cerebellum-mediated predictive control of an innate behavior

Sriram Narayanan[1], Aalok Varma[1], and Vatsala Thirumalai[1#]

[1]National Centre for Biological Sciences, Tata Institute of Fundamental Research, Bangalore 560065, India.

Keywords: internal models, Purkinje neurons, prediction error, zebrafish, optomotor, calcium imaging

Number of words: Abstract: 154, Introduction: 500, Results: 3395, Discussion: 993, Methods: 3386.
Number of Figures: 7
Number of Supplemental Figures: 8
Tables: 2
Videos: 2

#Corresponding author: vatsala@ncbs.res.in

Acknowledgements: The authors would like to thank the following sources of funding support: Wellcome Trust-DBT India Alliance Intermediate and Senior fellowships (VT), Department of Biotechnology (VT), Science and Engineering Research Board, Department of Science and Technology (VT), Department of Atomic Energy (VT), NCBS-TIFR graduate student fellowship (SN and AV). The authors would also like to thank Prof. Masahiko Hibi for providing the Tg(aldoca:GCaMP6s);nacre-/- fish line. Further thanks are also due to Mr. T.P. Jagadeesh for the maintenance of our fish lines and to Drs. Lena Robra, Mehrab Modi and Ebi George for providing advice and assistance. In addition we would like to thank the Central Imaging and Flow Facility at NCBS for support.

Abstract

The brain uses internal models to estimate future states of the environment based on current inputs and to predict consequences of planned actions. Neural mechanisms that underlie the acquisition and use of these predictive models are poorly understood. Using a novel experimental paradigm, we show clear evidence for predictive processing in the larval zebrafish brain. We find that when presented with repetitive optic flow stimuli, larval zebrafish modulate their optomotor response by quickly acquiring internal representations of the optic flow pattern. Distinct subcircuits in the cerebellum are involved in the predictive representation of stimulus timing and in using them for motor planning. Evidence for such predictive internal representations appears quickly within two trials, lasts over minute timescales even after optic flow is stopped and quickly adapts to changes in the pattern. These results point to an entrainment-based mechanism that allows the cerebellum to rapidly generate predictive neural signals ultimately leading to faster response times.

Introduction

Predictive processing is a widespread phenomenon in the central nervous system [1–6]. Behavioral output, in many cases, depends not only on sensory input and internal state, but also on the individual's understanding of how the world works [1,6–8]. The ability to predict future environmental states and consequences of actions is a fundamental element of cognition and enables complex actions to be planned in anticipation of the future [7,8]. Through experience, the brain acquires internal models which predict the consequences of actions [2,9,10], causes of sensory input [11] or future states of the environment [1,6]. The role of internal models in sensory perception [2,10,11] and motor command generation [5,12,13] has been extensively studied. Nevertheless, the neural circuit basis of how internal models are acquired and modified based on real-time inputs has thus far not been investigated extensively.

The cerebellum has been known to generate predictive signals that drive motor planning, learning and control [14–16]. Such predictive activity has been recorded from multiple cerebellar cell types and corresponds to motor [12,17–19] as well as non-motor functions [17,20–23]. A key element of internal models relates to predicting the timing of movements and sensory events and the cerebellum has been implicated in these functions [24–27]. However, such a timing function of the cerebellum is believed to be mostly in the sub-second to second range with relatively little contributions to the supra-second range [13,28]. Additionally, though the cerebellum is evolutionarily conserved across all vertebrates [29], a timing function of the cerebellum in lower vertebrates has thus far not been demonstrated. Here we show supra-second time-keeping in the cerebellum of larval zebrafish.

Larval zebrafish sense optic flow and generate compensatory swims (optomotor response or OMR), believed to help stabilize their position in flowing water [30,31]. The optomotor response generated is temporally specific, yet adaptable [32,33]. The behavioral relevance of optic flow to fish means that no prior training is required, giving us the opportunity to probe innate mechanisms that enable the cerebellum to acquire and use internal models to adapt to new environmental challenges. The larval zebrafish cerebellum has been shown to encode predictive pre-motor activity >10s before movements are made, indicating a role in motor planning [34]. Purkinje cells

in larval zebrafish perform a combination of sensory and motor functions [35] and are strongly activated by optic flow [35–37].

We placed zebrafish larvae in a one dimensional closed-loop optomotor track (Fig. 1a) [36,38], in which we imposed rhythmic on-off patterns of optic flow while simultaneously monitoring Purkinje cell activity. Occasionally, deviations were introduced in the pattern by not turning on optic flow as expected (Fig. 1b). We used these deviations to probe for behavioral and neural signatures of fish acquiring and using internal representations of the timing of optic flow stimulus. Our results demonstrate that distinct functional subcircuits in the cerebellum are involved in acquiring and updating internal representations of optic flow timing and in using them for motor planning.

Results

The cerebellum is required for expectation dependent trial by trial modulation of response latency

We placed 7-8 day old zebrafish larvae in a closed-loop optomotor track (Fig. 1a) and presented regularly timed optic flow stimuli to them (Fig. 1b). One trial consisted of an optic flow-on period of 2s followed by a 5s inter-trial interval (ITI) with no optic flow (Fig. 1b). During the optic flow-on period, the gain of the closed loop feedback was set to provide realistic visual feedback during swim bouts to maintain consistent levels of behavioral responsiveness [39]. Fish were presented with 100 trials out of which 10% of trials chosen pseudorandomly were probe trials, in which optic flow was not presented, resulting in a deviation from the predominantly experienced pattern (Fig. 1b). Probe trials were used to look for behavioral and neural signatures of fish using internal representations of their environment to predict the onset of optic flow and using predictions to plan behavioral responses to future optic flow-on events. The behavior setup was incorporated into a custom two-photon microscope to simultaneously image calcium activity in Purkinje cells during the behavior assay (Fig. 1a,c,d). Activity profiles of Purkinje neurons with respect to optic flow or probe trials were analysed offline (Fig. 1e).

Fish swam preferentially in the 2s optic flow-on periods and seldom during the 5s ITI when stationary gratings were presented, indicating that swim bouts were initiated in response to optic

flow (Fig. 2a,b). We then measured the latency to the first swim bout relative to the onset of optic flow (Fig. 1b), to look for indications that fish are predicting the onset of optic flow. Latency to respond to optic flow would be a function of pre-motor processing, unlike swim bout kinematics which are modulated within a bout using sensory feedback [32,40].

No swimming was observed in probe trials in the absence of optic flow (Fig. 2a,b). This shows that fish do not initiate swim bouts predictively and that swim bouts are gated by optic flow. Nevertheless, fish might still use predictive processes to generate swim bouts when optic flow is encountered as expected. We surmised that occurrence of a probe trial which deviates from the predominant stimulus pattern, might weaken such predictive processes. Therefore, we looked at whether a mismatch from expectation introduced by probe trials has an effect on latency in subsequent trials. We computed the fold change in latency in trials after a probe trial with respect to a pre-probe baseline (Fig. 2c) and saw that latency was significantly longer in the trial immediately following a probe trial and returned back to baseline by the next trial (Fig. 2d). The transient increase in latency induced by probe trials in these experiments suggests the involvement of a predictive component in generating swim bouts after optic flow onset.

To probe the role played by the cerebellum in using predictions to modulate latency, we laser ablated the cerebellum (Supplementary Fig. 1a,b) before performing the same behavior experiment as above. Probe trials did not cause a transient elevation in latency in cerebellum-lesioned fish (Fig. 2e). Other behavioral parameters were similar in lesioned fish compared to non-lesioned fish (Supplementary Fig. 1c-f). Both lesioned and non-lesioned fish showed similar levels of behavioral responsiveness (Supplementary Fig. 1c) and exhibited a drop in latency that developed slowly over the course of the experiment (Supplementary Fig. 1d-f). The cerebellum dependent elevation in latency caused by probe trials suggests a specific role for the cerebellum in modulating behavioral responses on a trial by trial basis, possibly employing a mechanism that uses predictions derived from internal representations of optic flow timing.

Purkinje cells encode a widespread, time-locked prediction error signal

To look for neural signatures of internal representations of environmental states, we simultaneously imaged calcium activity in Purkinje cells expressing GCaMP6s [41], using a custom

two-photon microscope. Calcium activity in a single optical plane with 69 ± 14 (mean ± SD , Supplementary Fig. 2) cells was recorded through each experiment, accounting for 15-20% of the total number of Purkinje cells at this stage of development [35,42]. Upon visual inspection, a significant fraction of cells showed a response to optic flow (Fig. 3a, left), caused by sensory input, motor activity or both. There was also a surprisingly widespread signal, time-locked to the expected optic flow-on time in probe trials (Fig. 3a, right) (Supplementary video 1). We then classified cells based on their average optic flow and probe responses using correlation based hierarchical clustering [43]. 5 distinct clusters, namely clusters 2, 3, 4, 5 and 8, were found based on the intersection of the independently generated optic-flow and probe response types (See Methods). 1573 out of all of the 1874 cells we recorded from could be classified into one of the 5 clusters. 954 out of 1573 cells belonged to cluster 4, with strong responses to optic flow and no response during probe trials (Fig. 3b-d). Clusters 2, 3, 5 and 8 showed large responses during probe trials (Fig. 3b). The probe responsive clusters also showed significant changes in activity during non-probe trials but their optic flow responses were significantly lower in amplitude than the probe responses (Fig. 3c). The mean response amplitude of cluster 3 cells during probe trials was similar to non-probe trials due to the lower response probability during probe trials (Fig. 3c,d). Probe triggered responses in all of the probe responsive clusters were time-locked to the expected onset time of optic flow (Fig. 3e, Supplementary Table 1). To further confirm that the probe responses were specific to the expected onset time of optic flow, we looked at all 1874 cells we recorded from, for any increase in activity in a window -2s to 4s from the onset of probe trials. An increase in activity was defined as any period of 1s within the window where the mean dF/F crossed 3 SDs above the pre-window baseline. A cell was chosen if it crossed the threshold in at least 3 probe trials. The responses we found using this method were also those tuned to the expected onset time of optic flow (Supplementary Fig. 3), confirming the temporal specificity of the probe response. These results clearly show that Purkinje cells encode a widespread and time-locked prediction error (PE) signal that is suppressed when predictions match reality during non-probe trials. Suppression of the PE signal is especially noticeable in cluster 2, where optic flow onset leads to a negative change in calcium activity when compared to pre-trial levels. This negative shift in GCaMP fluorescence is likely due to a reduction in activity in Purkinje cells with high rates of firing in the optic flow-off phase.

PE signals were encoded in Purkinje cell activity independent of motor activity (Supplementary Fig. 4,5). We used the total number of swim bouts and minimum latency as indicators of behavioral responsiveness. Minimum latency was calculated as the minimum value of the 10 trial moving average of latencies across all trials for each fish. Both these behavioral variables were highly anticorrelated, with fish that generated more swim bouts also showing lower minimum latencies (Supplementary Fig. 4c). Even relatively unresponsive fish had similar PE response probabilities (Supplementary Fig. 4a,b) and functional distribution of cells (Supplementary Fig. 5) to fish that were highly responsive. This indicates that Purkinje cells involved in encoding PE signals are performing a non-motor function and are involved in acquiring internal representations of the environment irrespective of whether motor output will be generated using them. PE response probability of cluster 4, although relatively much lower on average (Fig. 3d), showed weak but significant correlations with bout number and minimum latency (Supplementary Fig. 4a,b).

The existence of a robust, well timed PE signal points to a similarly robust and well timed internal representation of optic flow in the environment. To estimate the time course of acquisition of internal representations of optic flow timing, we looked at individual probe trials and calculated the probability of a cell exhibiting a PE signal and the amplitude of the signal when it occurred, without trial averaging (See Methods). Contrary to our expectation, neither probability nor amplitude of the PE signal showed an increase over the course of the experiment (Fig. 3f,g). The very first probe trial, presented after two consecutive trials of optic flow, had a PE signal indistinguishable from probe trials later in the experiment (Fig. 3f,g; Supplementary Fig. 6). The onset of the PE signal was rapid and did not change in probability or amplitude over the course of the experiment. Clusters 2, 3, 5 and 8 were pooled together for this analysis since we did not find differences between them.

Internal representations of optic flow are encoded in entrained neuronal activity

Based on key properties of the PE signal, its rapid onset, temporal specificity and suppression in non-probe trials, we hypothesized that the neural mechanism underlying this phenomenon involves a combination of entrained excitation with sensory tuned inhibition [44], where the entrainment represents the internal model of the environment.

The continued presence of a well timed optic flow response even after flow is stopped would be a clear indication of underlying entrainment, so would a PE response that remains across multiple probe trials. To test this, we presented a set of fish with multiple consecutive probe trials. In this experiment, fish were presented with 20 trials of optic flow of 2s duration with a 5s ITI, followed by 10 consecutive probe trials (Fig. 4a). Each experiment consisted of 5 repeats of this stimulus pattern, with no gaps in between them. We then filtered cells with three broad response properties using regressors made by convolving the stimulus waveform with a GCaMP6s kernel [45]. Three regressors were made, the first one representing the optic flow stimulus, the second representing a response to optic flow that remains entrained during the extended probe phase and the third representing an entrained PE signal that is suppressed during the optic flow-on phase (Supplementary Fig. 7a-top). These response profiles broadly represent the clusters observed in Fig. 3. Cells were classified based on cross correlation with the three regressors as optic flow driven, entrained or PE with a threshold correlation coefficient of 0.3 required for classification (Supplementary Fig. 7a-bottom). A significant fraction of cells could be classified into the three groups, with 30 ± 5 (mean ± SD) cells showing a strong optic flow response and no PE signal, 2 ± 2 cells showing an entrained response and 6 ± 2 cells showing an entrained PE signal (Fig. 4a) (Supplementary Fig. 7a-c) (Supplementary video 2). The entrained PE signal remained time-locked to the expected onset times of optic flow in each of the 10 probe trials (Fig. 4b) (Supplementary Table 2). The PE signal also remained robust across the 10 probe trials with comparable response probabilities and amplitudes across the 10 probe trials (Fig. 4c,d). Statistically, the PE response probability showed a weak but significant decay from the first trial compared to baseline (Fig. 4c) ($p = 0.022$, Wilcoxon signed-rank test, 10 fish). No other trials showed significantly different response probability compared to baseline. Similarly, the PE response amplitude showed weak but significantly elevated values over baseline in trials 2 and 4 (Fig. 4d) ($p = 0.028$ and 0.017 respectively, Wilcoxon signed-rank test, 10 fish). No trend was observed over the 5 repeats in mean response probability or amplitude (Fig. 4e,f). Baseline was estimated as the mean value closest to the 25th percentile of all means for the above analysis.

Since by definition, cells with high correlation coefficients with optic flow or PE regressors are likely to have high correlation with the entrained response regressor, we classified cells as entrained only if they had suprathreshold entrained correlation and subthreshold optic flow and

PE correlations (Supplementary Fig. 7a-bottom, d-f). Out of the cells that showed entrained responses, the responses were either more 'optic flow like' or 'PE like' (Supplementary Fig. 7g-i). We did not investigate them further due to the low number of cells (Supplementary Fig. 7b, g-i).

For a predictive mechanism to be useful, it should be able to adapt to changes in the environment. We tested the adaptability of the internal model by varying the ITI after 60 trials from 5s to 7s, without any additional gap between the two blocks of 60 trials. We selected cells that showed at least one PE signal for the 5s ITI and looked at probe triggered averages for these cells during the 7s ITI. The PE signal tuned to the 5s ITI switched to the 7s ITI by the first probe trial (Fig. 4i,j). The first probe trial following the switch in ITI was either the fourth or eighth trial post switch.

Results from the above experiments provide conclusive evidence for an entrainment based mechanism in predicting optic flow timing. The entrainment continued for at least 70s without sensory cues, with a detectable but small decay in strength, but is capable of rapidly adapting to new intervals to match changes in the environment.

Electrophysiological analysis of PE signals and pre-trial predictive responses in Purkinje cells

In order to identify the input sources to Purkinje cells contributing to PE signals and possibly predictive signals used to plan motor commands, we performed loose-patch recordings from paralyzed fish that were engaged in the same behavior assay as shown in Fig. 1b (Fig. 5a). Purkinje cells receive excitatory inputs from two sources, climbing fibers (CFs) from the inferior olive and parallel fibers (PFs) from cerebellar granule cells. CFs have been shown to encode error signals [12] and other complex features important for behavioral tasks, like expectation of learnt events [20,21]. PFs convey to Purkinje cells a rich representation of the sensorimotor environment and also learnt predictive signals [19,23,46]. Single CF inputs cause large, easily detectable changes in GCaMP fluorescence in Purkinje cells whereas PF mediated changes in simple spike (SS) rates contribute to a much smaller fraction of the GCaMP signal [35,47].

A significant elevation in CF rates compared to baseline was observed in probe trials in 5 out of 18 cells (Fig. 5b,c), with these cells also showing high modulation indices : 0.51 ± 0.31 (Mean ± SD). 2 cells showed significant elevation in SS rates compared to baseline (Fig. 5b,d), but with very low modulation indices : 0.09 ± 0.007 (Mean ± SD). No statistical testing was done to further analyse the SS rate increase in probe trials as the modulation indices were negligible and were unlikely to cause the large amplitude PE signals observed in calcium imaging. These results strongly indicate that PE signals are encoded in CF inputs to Purkinje cells which result in the large calcium responses seen in probe trials.

Next, we looked at non-probe trials for a pre-trial increase in CF and SS rates, which could possibly represent an entrained predictive signal. All cells showed positive SS modulation indices during optic flow compared to baseline (Fig. 5e,f). CF inputs were positively modulated by optic flow in 14 out of 18 cells (Fig. 5e,g) and strongly negatively modulated in the remaining 4 cells (Fig. 5e,j). We separated cells based on the sign of their modulation index for further analysis. Both CF and SS rates in cells with positive modulation indices showed a significant pre-trial ramp (Fig. 5h,i) leading up to the onset of the trial and could possibly represent an entrained predictive signal. Cells with negative CF optic flow modulation indices showed high pre-trial CF rates that were suppressed almost completely by optic flow (Fig. 5j). The suppression was absent in probe trials (Fig. 5j) and occurred significantly before the onset of motor activity (Fig. 5k), indicating a possible role for these cells in optic flow timing, rather than motor control.

These results strongly indicate that PE signals are encoded in CF inputs from the inferior olive. The pre-trial increase in both SS and CF rates seen here possibly represents predictive processes involved in optic flow timing or motor planning.

Predictive signals encoded by Purkinje cells correlate with latency at the single trial level

Thus far, we have shown that Purkinje cell activity encodes predictive and prediction error signals when repeating optic flow stimuli are presented. To analyse how the cerebellum uses this predictive information to modulate behavioral responses to optic flow, we independently looked at how both PE signals and entrained pre-trial activity correlate with latency on a trial by trial

basis. For this analysis, we used data from experiments shown above in Fig. 2 and 3. First, we hypothesized that robustness of the PE signal during a probe trial reflects the robustness of the internal representation used to plan behavioral responses in non-probe trials near that probe trial. The probability of occurrence of PE signals across the cells we imaged varied from trial to trial. For example, Fig. 6a shows the same cells imaged in two trials, with the trial shown on top having a PE response probability of 0.26 while the one shown in the bottom has a PE response probability of only 0.04. We linearly interpolated the PE probability between probe trials to obtain an indirect, coarse grained estimate of the robustness of internal representations. We then computed the correlation coefficient between the interpolated PE probability and latency. Latencies were also linearly interpolated and smoothened with a rolling average of 10 trials before computing the correlation coefficient. The 10 trial smoothing window matches the average distance between probe trials, thereby yielding a comparably coarse grained estimate of latency (Fig. 6b). Fish that paused swimming for >10 consecutive trials at any point during the experiment were excluded to minimize interpolation artifacts. 12 out of 16 fish showed significant negative correlations between interpolated PE probability and latency compared to chance. Out of the remaining 4 fish, 2 showed significant positive correlations and 2 fish did not show significant correlations. Overall, the population showed a significant negative correlation between interpolated PE probability and latency (Fig. 6b,c). These results show that robust PE signals observed during probe trials, indicative of a strong internal representation of optic flow timing, are associated with lower latency to respond during optic flow trials. This also strongly suggests that predictive information might be used to plan motor commands to be executed when optic flow is encountered as expected.

Observations from loose-patch recordings show an entrained pre-trial increase in SS and CF rates that could potentially be involved in motor planning (Fig. 5h,i). To test whether the entrained component prior to the onset of optic flow is involved in modulating behavioral responses, we looked at whether the average population activity in the calcium imaging frame prior to the onset of optic flow predicted latency from trial onset. The pre-flow population activity averaged across all cells showed a significant negative correlation with latency from trial onset (Fig. 6d). There was no correlation when trial order was shuffled (Fig. 6e). To get a better understanding of what functional cell types were involved, we grouped cells into the functional

clusters identified earlier (Fig. 3b) and looked at clusterwise correlations between pre-flow population activity and latency. The pre-flow population activity in cluster 4 was responsible for the correlation observed when all cells were pooled together (Fig. 6f,g). Cells in cluster 4 show large calcium responses to optic flow and do not show PE signals (Fig. 3b,d). Significant predictive information about latency was present in pre-flow population activity in cluster 4 upto 2.5s prior to the onset of a trial (Fig. 6h), indicating that these cells are involved in motor planning well before the onset of optic flow. This is consistent with the observation from loose-patch recordings where an entrained increase in SS and CF rates was observed seconds before trial onset (Fig. 5h,i). There was no correlation when we independently tested the other clusters (Supplementary Fig. 8).

These results reveal two distinct functional subcircuits in the cerebellum, one that encodes predictive activity entrained to stimulus patterns in the environment (cluster 4) and another that manifests an error signal when the expected stimulus does not occur (clusters 2, 3, 5 and 8). On a trial-to-trial basis, the entrained predictive activity feeds into motor planning resulting in faster behavioral responses while the error signals are used to update internal models that are no longer valid.

Discussion

Our results show conclusive evidence that larval zebrafish acquire internal models of temporal patterns in optic flow in their environment over timescales of several seconds (Fig. 3a,b). The internal model is used to predictively plan optomotor responses to expected changes in optic flow in the environment (Fig. 6). Fish acquire an internal representation of optic flow timing with the minimum evidence possible, i.e. in 2 trials (Fig. 3f,g) (Supplementary Fig. 6). To our knowledge, this form of one-shot learning has not been shown in larval zebrafish before and highlights the inherent ethological significance of optic flow. Shallow water streams inhabited by larval zebrafish often show locally periodic changes in flow due to water waves or vortex streets shed by objects intercepting laminar flow. Fast and precise reactions to these perturbations caused by flowing water is likely to prevent fish from being washed away from a favourable environmental niche. Apart from being acquired rapidly, we show that the internal model is readily adaptive to sudden changes in periodicity (Fig. 4g,h), making it highly relevant in the

natural setting. In addition to this homeostatic function, it is possible that fish incorporate predicted environmental perturbations to fine tune other behavioral responses such as escape swims or prey capture maneuvers.

Observations from experiments in which fish were presented with multiple consecutive probe trials show that the internal representations are encoded in entrained excitatory activity (Fig. 4a,b). The mechanism of acquisition of entrainment remains to be investigated. It is conceivable that entrainment is encoded by a set of reciprocally connected neurons forming an oscillatory circuit similar to those seen in central pattern generators [48]. The periodicity of this hypothetical circuit could be dynamically tuned over behavioral timescales by synaptic and/or neuromodulatory inputs [49]. A similar reciprocally connected oscillatory circuit in the fish hindbrain has been implicated in controlling turning behavior [50] and in biasing turns to navigate gradients [51]. Such a mechanism also fits in with the rapid acquisition and adaptability we see with the internal model.

Both entrained predictive signals and error signals are encoded in Purkinje cell activity in the cerebellum. The entrained pre-trial increase in SS and CF rates seen in Purkinje cells (Fig. 5h,i) indicates that the internal representations of optic flow are encoded in sensory areas upstream of the cerebellum. The pretectum and optic tectum have been shown to be involved in visual processing linked to the optomotor response [52–54] and cells in the optic tectum have previously been shown to entrain to rhythmic visual stimuli [55], making them compelling candidate regions that encode entrained internal representations of optic flow (Fig. 7a). The entrained internal representations in sensory areas of the brain would enable fish, in some sense, to 'see into the future', and a subcircuit in the cerebellum uses this predicted visual information to plan optomotor responses to future optic flow-on events (Fig. 2d,e , Fig. 6d-h). In parallel, a distinct subcircuit of Purkinje cells is involved in acquiring and updating internal representations of optic flow, possibly by sending appropriate feedback signals to sensory areas that encode these representations [56] (Fig. 7a). Purkinje cells that are part of this parallel circuit exhibit PE signals (Fig. 3b , Fig. 6d-h).

Results from our experiments (Fig. 3b,c , Fig. 5b-d), put together with previous characterization of Purkinje cell calcium responses [35,47], strongly suggest that PE signals are encoded in CF inputs to Purkinje cells. This would mean that error signals are present and are possibly computed in the inferior olive [12,57] (Fig. 7a). The widespread presence of PE signals in the Purkinje cell population underlines the central role played by the cerebellum in acquiring and updating internal representations of the environment over supra-second timescales. Based on the observation that PE signals are suppressed in non-probe trials (Fig. 3b,c , Fig. 4e), a likely explanation for the underlying mechanism that generates them is a combination of sensory tuned inhibition with entrained excitation (Fig. 7a). Excitatory predictions and inhibitory sensory inputs combining to generate mismatch signals [44] is a central component of the predictive coding framework [58]. Such parallels across model systems are extremely insightful as they can potentially reveal fundamental principles of brain function, in this case, those performing core computations required for predictive coding.

Additionally, these results uncover a novel, purely non-motor role for the cerebellum, where it is involved in acquiring internal representations of the environment, independent of motor activity (Supplementary Fig. 4,5). The fish cerebellum is innately capable of acquiring predictive signals, with exposure to two well timed repetitions of optic flow events (Fig. 3f,g) (Supplementary Fig. 6). The internal representations of optic flow are acquired irrespective of whether they are eventually used to predictively modulate optomotor responses, with relatively unresponsive fish exhibiting robust PE signals indistinguishable from highly responsive fish (Supplementary Fig. 4,5). This extends recent findings which show that apart from performing motor control functions, the cerebellum acquires task relevant predictive responses [14,16,19–21,23,34] and is involved in motor planning through cortical feedback loops [14,16,17,24]. Predictive functions performed by the fish cerebellum are likely to be highly adaptive to a variety of contexts [34,59] and may be capable of acquiring more complex internal models of the world. The rich multimodal sensory representations converging onto Purkinje cells [46,60] make the cerebellum a potential hub for acquisition of models of the environment that span arbitrary combinations of sensory modalities.

To summarize, we show how larval zebrafish acquire and use internal representations of rhythms in optic flow in their environment to predictively modulate optomotor responses. These findings

add a new dimension to our understanding of behavior generation algorithms employed by larval zebrafish. The role of the cerebellum and feedback loops formed with sensory areas of the brain are likely to be conserved across organisms and further investigation can provide mechanistic insight into the fundamental principles of how brains adaptively internalize rules of the world.

Methods

Fish

We used 6-8dpf zebrafish (*Danio rerio*) larvae for all experiments. The larvae were raised in E3 medium (composition in mM: 5 NaCl, 0.17 KCl, 0.33 CaCl2, 0.33 MgSO4, 0.5 methylene blue) at 28.5°C in accordance with standard protocols (https://zebrafish.org/home/guide.php). Tg(aldoca:GCaMP6s) ; nacre -/- larvae (from Prof. Masahiko Hibi, Nagoya University, Japan), outcrossed into the Indian wildtype (from local aquarium suppliers) background were used for experiments involving two-photon imaging. Indian wildtype larvae were used for electrophysiological recordings. All experimental procedures were approved by the Institutional Animal Ethics Committee of the National Centre for Biological Sciences.

Experimental preparation

For experiments involving two-photon imaging, 7-8dpf zebrafish larvae were anaesthetized by briefly immersing them in 0.017% MS222 (Sigma-Aldrich) and embedded dorsal side up in a drop of 2% low gelling temperature agarose (Sigma-Aldrich) placed in the center of a 60mm petri dish lid. The dish was filled with E3 medium and the tail below the level of the swim bladder was freed from agarose. The embedded fish were allowed to recover for 4-8 hours before the experiment.

Real-time motor output detection for closed-loop optomotor feedback

Custom Bonsai workflows [61] were used for real-time motion detection. The algorithm used by our software for online motion detection closely matched previously published protocols [36,38]. Video based motion detection was done at 200fps using a Flea3-USB3.0 camera (FLIR). The tail of the fish was illuminated from one side by a collimated 780nm LED (M780D2, Thorlabs) and imaged onto the camera sensor below (Fig. 1a), using a reversed Nikon 50mm f/1.8d lens with a 24mm extension tube for increased magnification. Both the illumination and imaging light paths

were filtered through 780nm bandpass filters (FBH-780-10, Thorlabs). The imaging light path was filtered to exclude light from the visual stimulus and two-photon laser and the illumination light path was filtered to block low intensity visible light emission from the 780nm LED. Real-time motion detection was performed by frame subtraction. The fraction of motion pixels in each frame, which scales with the amount of tail movement, was lowpass filtered with a 10ms time constant to obtain the instantaneous swim strength (ISS). This lowpass filter simulates the inertial effects experienced by larval fish in water. The ISS was streamed in real-time using Open Sound Control (OSC) protocol to custom software written in Processing 2.2.1 (https://processing.org/). This software generated visual stimulus, executed the experimental protocol, and generated TTL signals to synchronize two-photon imaging or electrophysiology data acquisition.

ISS for the electrophysiology preparation was estimated from fictive swims recorded unilaterally from the ventral root. Analog output from the recording amplifier was digitized at 12KHz in 10ms chunks (PCIe-6361, National Instruments) and acquired using a Bonsai workflow. Each 10ms chunk was bandpass filtered between 0.2-5kHz. The standard deviation of each chunk was calculated and the offset induced by recording noise was subtracted. This signal was lowpass filtered at 10Hz and thresholded manually to obtain an estimate of the ISS, which was streamed to the experiment control software.

The ISS was scaled individually for each fish to obtain a realistic estimate of swim velocity. 1-3 trials of optic flow at 10mm/s lasting 10-15s were presented before the start of each experiment in the open-loop configuration. A scaling factor, s, was calculated from these trials such that the ISS when scaled resulted in an average swim bout velocity of 15mm/s. This process is described by the following equation.

$$vswim_n = s \times g \times ISS_n$$

Where *n* is the frame count. *vswim* is the instantaneous velocity of the fish in the closed-loop environment. *s* is the scaling factor set individually for each fish. *g* is the gain of the closed-loop feedback, set at 1.0 for all experiments. *ISS* is the instantaneous swim strength.

Visual stimulus

Custom software written in Processing 2.2.1 was used to control the experimental protocol as well as to generate and update the visual stimulus at 120Hz. The visual stimulus consisted of square wave grating with a spatial period of 10mm presented 5mm beneath the fish. During optic flow-on phases, the grating drifted at 10mm/s in the tail to head direction. Motor output of the fish during the optic flow-on phases resulted in realistic deceleration and a smooth change in direction of optic flow based on the following equation.

$$vgrating_n = vflow_n - vswim_n$$

Where $vgrating_n$, $vflow_n$ and $vswim_n$, are the instantaneous velocities at frame *n* of the grating stimulus, externally imposed optic flow and the fish respectively.

In the calcium imaging setup, visual stimulus was projected on a 60mm diameter diffusive paper screen placed 5mm below the fish. The projector was custom built around a 5-inch LCD panel (Adafruit) removed from its housing. The LCD was illuminated from behind with a collimated 617nm LED (Luxeonstar) and was imaged onto the projection screen. A custom made driver was used to power the LED antiphase to the linescans of the fast x-galvo during two-photon imaging. This eliminated the possibility of bleedthrough of light from the visual stimulus into the calcium imaging channel. In addition to this, a longpass filter (575lp, Chroma) was placed in the projection light path to prevent harmful levels of light from reaching the PMT. The final pixel size on the projection screen was 0.32mm. A 5X5mm window was cut out in the projection screen to facilitate video recording of tail movements from below. Visual stimulus for the electrophysiology experiments was presented directly on an LCD screen positioned beneath the fish.

Behavior assays

Fish were placed in a one-dimensional closed-loop optomotor track as described above. They were presented with repetitive trials of optic flow with a trial duration of 2s, which was kept constant for all experiments. The inter-trial-intervals (ITIs) were 5s long, unless specified otherwise. Gratings were stationary in the ITIs. 10% of trials chosen pseudorandomly were probe trials, in which optic flow was not presented (Fig. 1b). The pseudorandom distribution was set such that one trial was chosen to be a probe trial for each 10 trial chunk of the experiment. Each fish was presented with 100 trials and were previously not exposed to rhythmic changes in optic flow. Only fish that were behaviorally responsive by generating at least 1 swim bout during the pre-experiment scaling process described above were put through the rest of the experimental protocol.

To test for underlying entrainment to the timing of optic flow, we presented each fish with a block of 20 consecutive trials with 5s ITIs, without probe trials, followed by 10 consecutive probe trials with the same 5s ITIs. Each fish was presented with 5 repeats of this trial structure (Fig. 4a-h).

Adaptability of internal representations was tested by changing the ITI during the experiment (Fig. 4i,j). In these experiments, fish were initially presented with 60 trials of optic flow with 5s ITI after which the interval was switched to 7s for another 60 trials, with no gap in between the two sets of 60 trials.

In electrophysiology experiments, fictive motor recordings were obtained from 9 out of 18 fish. Closed-loop feedback was provided for those fish and the remaining 9 fish went through the experimental protocol without closed-loop feedback. Data from both groups were pooled together.

Two-photon calcium imaging

Head-restrained tg(aldoca:GCaMP6s) ; nacre -/- larvae were used for all experiments. Imaging was performed on a custom two-photon microscope controlled using ScanImage 3.8 [62]. A Ti-Sapphire laser (Chameleon Ultra II, Coherent) tuned to 920nm was used to excite GCaMP6s

using a laser power of 20-30mW at the sample plane. The laser was focussed at the sample using a 20X 1.0NA objective lens (Olympus), downstream of 50mm and 300mm focal length scan and tube lenses (AC-300-050B and AC-508-300-B, Thorlabs). Scanning was achieved using 3mm aperture scan mirrors (6215H, Cambridge Technology). A single 512X128 pixel field of view with 0.53µm pixel size, centred around the Purkinje cell layer was scanned using a pixel dwell time of 1.6µs, resulting in a frame rate of 7.8Hz. Fluorescence emission from GCaMP6s was detected with a GaAsP PMT (H7422PA-40, Hamamatsu). Output from the PMT was amplified using a preamplifier (SR570, Stanford Research Systems) and acquired using the same data acquisition card used to drive the scan mirrors (PCI-6110, National Instruments). Data acquisition from the microscope was triggered by a TTL pulse generated by an arduino connected to a separate computer running the behavior protocol. We acquired a continuous timeseries of two-photon images for each fish, spanning the duration of the experimental protocol.

Two-photon laser ablations

Tg(aldoca:GCaMP6s) ; nacre -/- larvae were prepared for cerebellum ablations using the same protocol as used for the calcium imaging experiments. 10 planes within the Purkinje cell layer, separated by 4µm, were serially scanned with the same scanning parameters used for the imaging experiments. Ablations were confined to the Purkinje cell layer using visual aid from GCaMP fluorescence. The laser was tuned to 920nm with a power of ~230mW at the sample plane. Each plane was scanned 10 times before moving to the next. This led to effective plasma based lesioning of the whole cerebellum within the region being scanned. Lesions were confirmed visually by an immediate increase in fluorescence intensity due to uncontrolled influx of calcium into the cytosol, followed by blebbing and disintegration of cells. Fish were allowed to recover for 1 hour post lesion before initiating the behavior protocol. The cerebellum was scanned while the behavior protocol was carried out, with laser power and scan settings identical to those used for calcium imaging in non-lesioned fish to maintain experimental conditions.

Electrophysiology

6-7dpf zebrafish larvae were first anesthetized in 0.01% MS-222 and transferred to a recording chamber. Two pieces of fine tungsten wire (California Fine Wire) were used to pin the larvae

through the notochord onto a Sylgard (Dow Corning) slab in the recording chamber. A third pin was used to orient the head dorsal side up (Fig. 5a). The MS-222 was then replaced by external solution (composition in mM: 134 NaCl, 2.9 KCl, 1.2 MgCl2, 10 HEPES, 10 glucose, 2.1 CaCl2, 0.01 d-tubocurarine; pH 7.8; 290 mOsm) and the skin covering the brain and along the tail was carefully removed using forceps (Fine Science Tools). The preparation was then taken to a rig apparatus.

Patch pipettes for loose patch recordings were made using thick-walled borosilicate capillaries (1.5 mm OD; 0.86 mm ID, Warner Instruments) and pulled to 1-1.5 µm tip diameter using a Flaming Brown P-97 pipette puller (Sutter Instruments), such that their resistance when backfilled with external solution was approximately 7-10 MΩ. Similarly, suction recording pipettes for fictive motor recordings were made using thin-walled borosilicate capillaries (1.5mm OD; 1.1mm ID, Sutter Instruments), pulled to ~5 µm tip diameter, such that their resistance when backfilled with external solution was ~0.7-1.5 MΩ.

First, ventral root recordings to monitor fictive swimming were obtained by guiding the pipette to a myotomal boundary (~15-20th somite) and applying mild suction. Once a successful recording was obtained, the focus was shifted to the cerebellum and loose patch recordings from Purkinje neurons were obtained. The pipettes were guided visually using the 60x/1.0NA water immersion objective of a compound microscope (Ni-E, Nikon) and a motorized micromanipulator (PatchStar, Scientifica). Once both recordings were obtained, the condenser of the microscope was gently moved to allow the introduction of a 5-inch LCD screen (Adafruit) to present visual stimuli. Recordings were included for analysis only if their quality did not deteriorate before at least 5 probe trials were presented.

Visual stimulus presentation and electrophysiological recordings were triggered simultaneously and acquired using a Multiclamp 700B amplifier, Digidata 1440A digitizer and pCLAMP software (Molecular Devices). The data were low-pass filtered at 2kHz using a Bessel filter and sampled at 50kHz at a gain between 10-2000, adjusted depending on the quality of each recording. The ventral root recordings were parallely acquired and real-time analysis was performed to provide closed-loop optomotor feedback as described above.

Data processing and analysis

Data processing and analysis was done primarily using Python (python.org). Both Python and MATLAB (Mathworks) were used for analysis of electrophysiology data.

Behavior data processing

Swim velocity data and timestamps saved from the experiment control software at ~120Hz were used for estimating latency (Fig. 1b). A simple threshold was sufficient to detect the beginning and end of swim bouts as signal to noise ratios were sufficiently high.

Latency modulation around probe trials

Latency modulation around probe trials was estimated by determining the fold change in latency relative to baseline latency in each trial for a 10 trial window around a probe trial (Fig. 2c-e). The baseline was determined as the mean latency observed over 5 trials before the probe trial. This normalization was necessary as slow drifts in latency developed over the duration of the experiment (Supplementary Fig. 1). Trials were selected if there were at least 3 swim bouts on either side of the probe trial. A minimum of 3 such trials were required per fish to obtain an average latency modulation trace for that fish. These criteria were pre-selected before the analysis was performed and the statistical inference did not change when we later varied the selection criteria to include probe trials with at least 1 swim bout on either side. 17 out of 27 fish passed this exclusion criteria and are represented in the analysis shown in Fig. 2d,e.

Calcium trace extraction

Calcium traces were extracted from individual Purkinje cell somata using a semi-automated processing pipeline written in Python. The images were corrected for translation along the X-Y plane using phase correlation with the registration module in scikit-image [63]. After motion correction, the centres of individual cells were identified manually using a GUI. A three layer neural network trained using a subset of data from these experiments was used to mark cell boundaries, guided by the manually identified centre coordinates. Pixels within the ROI were averaged to obtain fluorescence intensity of each cell for a given frame. Fold change in fluorescence intensity over baseline (dF/F) was calculated with baseline estimated as the tenth

percentile of a one minute window around each frame. Overlapping pixels assigned to more than one ROI were excluded from any of the assigned ROIs to avoid signal contamination from neighbouring cells. The resultant ROIs consisted of 140 ± 26 (mean ± SD) pixels each.

Hierarchical clustering

Correlation based hierarchical clustering was used to group cells based on functional response types. 1874 cells from 27 fish were pooled for clustering. This clustering step was done separately for optic flow and probe triggered average responses of all cells. The number of clusters was determined by a threshold for linkage distance between clusters. This threshold was chosen manually from a dendrogram and matched automated estimation using elbow plots. 3 functional clusters each were found for both optic flow and probe triggered responses. We then subdivided clusters by finding the intersections of each of the optic flow and probe response clusters, resulting in a total of 9 potential clusters based on both optic flow and probe response properties. Any cell with a Pearson's correlation coefficient less than 0.3 with the mean response profile of that cluster was excluded from the cluster. Out of these 9 potential clusters, 4 were disregarded from further analysis as the number of cells averaged less than 1 per fish. Cluster numbers 2, 3, 4, 5 and 8 were taken for further analysis and contained 175, 175, 954, 179 and 90 cells respectively.

Due to the short 2s duration of each trial, motor responses could not be reliably distinguished from optic flow responses in the triggered average traces. Cells involved in motor command generation will be classified by this method as optic flow responsive due to the high correlation between optic flow and motor output.

Estimation of PE response probability and amplitude

For analyses involving single trial estimation of PE responses, calcium traces without trial averaging were evaluated for a significant increase in fluorescence in probe trials. A response was considered significant if the mean fluorescence intensity of a 1s window centered around the end of a probe trial was greater than the mean fluorescence intensity of the 1s window preceding the onset of that probe trial by at least 3 SDs of the pre-trial levels. The average dF/F of the 1s window around the end of a probe trial is referred to as the PE response amplitude. The number

of probe trials in Fig. 3f,g is greater than 10 since we presented multiple groups of fish with different sets of 10 pseudorandomly chosen trials as probe trials (3 groups of 5, 7 and 15 fish).

Both PE response probability and amplitude were calculated for individual probe trials across cells and for individual cells across all probe trials. These can be distinguished by the labels 'Trial-wise' or 'Mean' PE probability/amplitude respectively in the figures. In all cases, error bars represent variability across fish as described in the figure legends.

Analysis of PE response onset

Onset times were estimated using the average response profile of the signal of interest for each fish. The onset time was determined as the time point of maximum slope, where the slope was estimated for each time point with respect to the value 5 calcium imaging frames in the future. A randomization based test was used to determine whether the variance of the onset time distribution across fish is significantly lower than expected by drawing random samples of equivalent sample size from a uniform distribution [3]. P-values were estimated from the number of times, out of 10^6 runs, the variance of random samples was lower than the variance of the onset time distribution. A significantly lower variance indicates temporal specificity of response onsets.

Spike detection and analysis

Spikes were identified as events that showed large fluctuations relative to a 25ms rolling window baseline and the peak times and amplitudes were extracted. Small amplitude events were classified as simple spikes (SSs) and large amplitude events as climbing fiber (CF) inputs [57]. Once identified and sorted, recordings were triggered to the start of optic flow trials or probe trials. Mean firing rates for optic flow and probe trials were estimated by convolving peri-event time histograms of 20ms binwidth with a 200ms gaussian kernel. Analysis was done using custom scripts written in Python and CF/SS event detection was done in MATLAB (https://github.com/wagenadl/mbl-nsb-toolbox).

Modulation indices were calculated for each kind of event (CF and SS) using the following formula:

$$modulation\ index = \frac{mean\ event\ rate - mean\ baseline\ event\ rate}{mean\ event\ rate + mean\ baseline\ event\ rate}$$

Where the mean event rate is the mean CF or SS rate during the 2s trial period and the mean baseline event rate is the mean event rate in the 2s window prior to trial onset. The modulation index has a range of -1 to 1 with positive values for an increase in event rate during a trial compared to baseline and negative values for a reduction in event rate.

Analysis of event rate modulation in probe trials

Each cell was evaluated independently for a significant increase in CF or SS event rates during probe trials. We randomly sub-sampled trials from non-probe trials 1000 times and estimated the mean baseline event rates for each sub-sampled group of trials. The number of sub-sampled trials in each group was equal to the number of probe trials for that cell. The distribution generated by repeated sub-sampling gives us an estimate of the inherent variability in event rate estimates when trial counts are low, as is the case for probe trials. If the mean event rate during probe trials was greater than the mean + 2 SD of the random, sub-sampled distribution, the increase was considered significant.

Statistics

All tests were performed in Python using SciPy [64] and Statsmodels [65]. The statistical tests used and their results are mentioned in the figure legends. In cases where linear mixed-effects models were used, we selected either random intercept or random intercept and slope models, based on which one of the two models resulted in a better fit as indicated by a higher log-likelihood value. In all cases, linear mixed-effects models were used to evaluate the significance of slope.

Figures

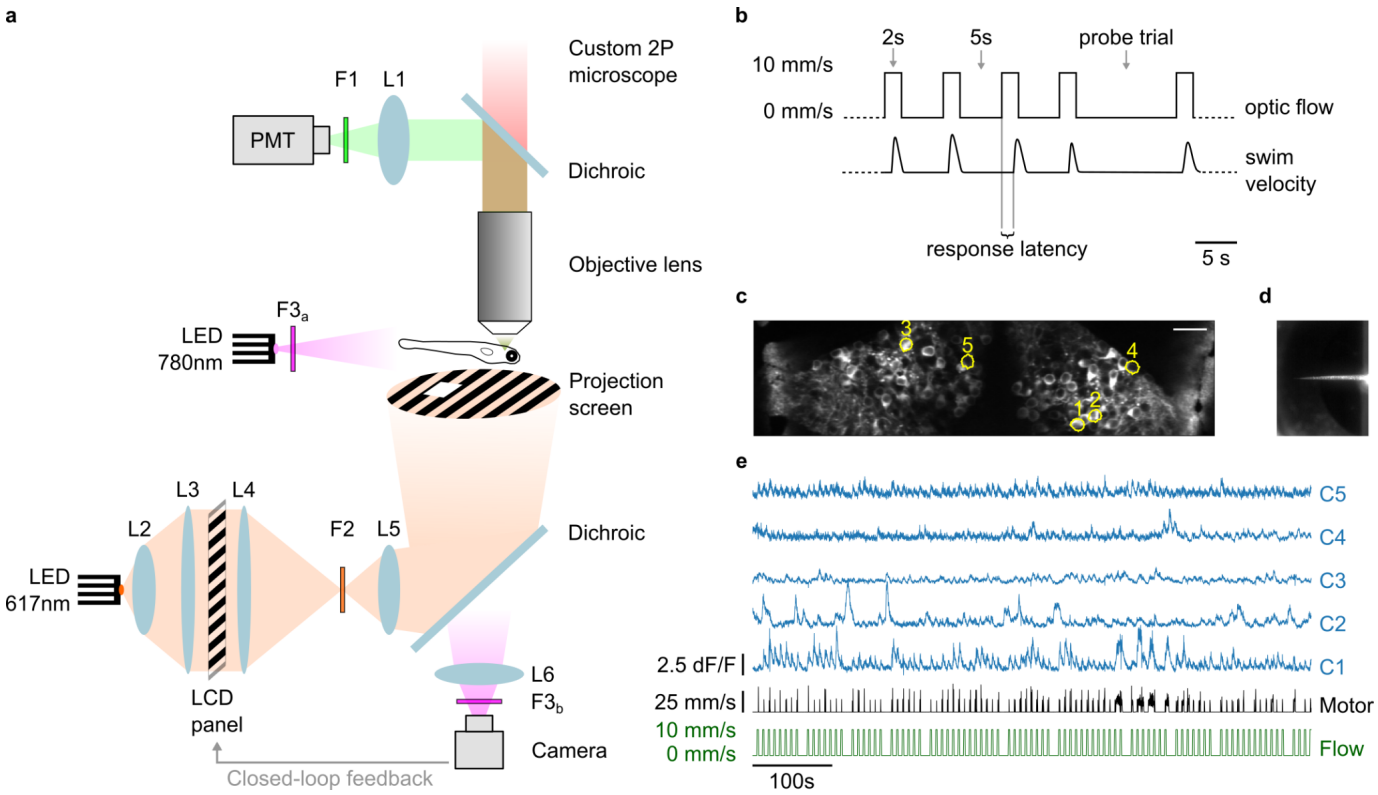

Fig.1: Sensory prediction assay for larval zebrafish.

a, Schematic of the custom built experimental setup. A head restrained 7dpf zebrafish larva is placed in a closed-loop optomotor track underneath a two-photon microscope. L1-6 : convex lenses, F1-3 optical bandpass filters (See Methods). **b,** A cartoon of the experimental protocol. Each trial is 2s long followed by a 5s inter-trial interval. 10% of trials chosen pseudorandomly are probe trials in which optic flow is not turned on, resulting in a deviation from the predominantly imposed pattern. Latency to respond to optic flow in each trial is taken as the behavioral readout. **c,** Average image of a single optical plane of Purkinje cells specifically expressing GCaMP6s under the aldoca promoter. Scale bar : 20µm. **d,** A video grab from the closed-loop camera showing the tail of a head restrained fish while two-photon imaging was being carried out. **e,** Example calcium imaging traces (blue) from 5 cells (ROIs marked in **c**) aligned to motor output (black trace) and the optic flow stimulus (green trace).

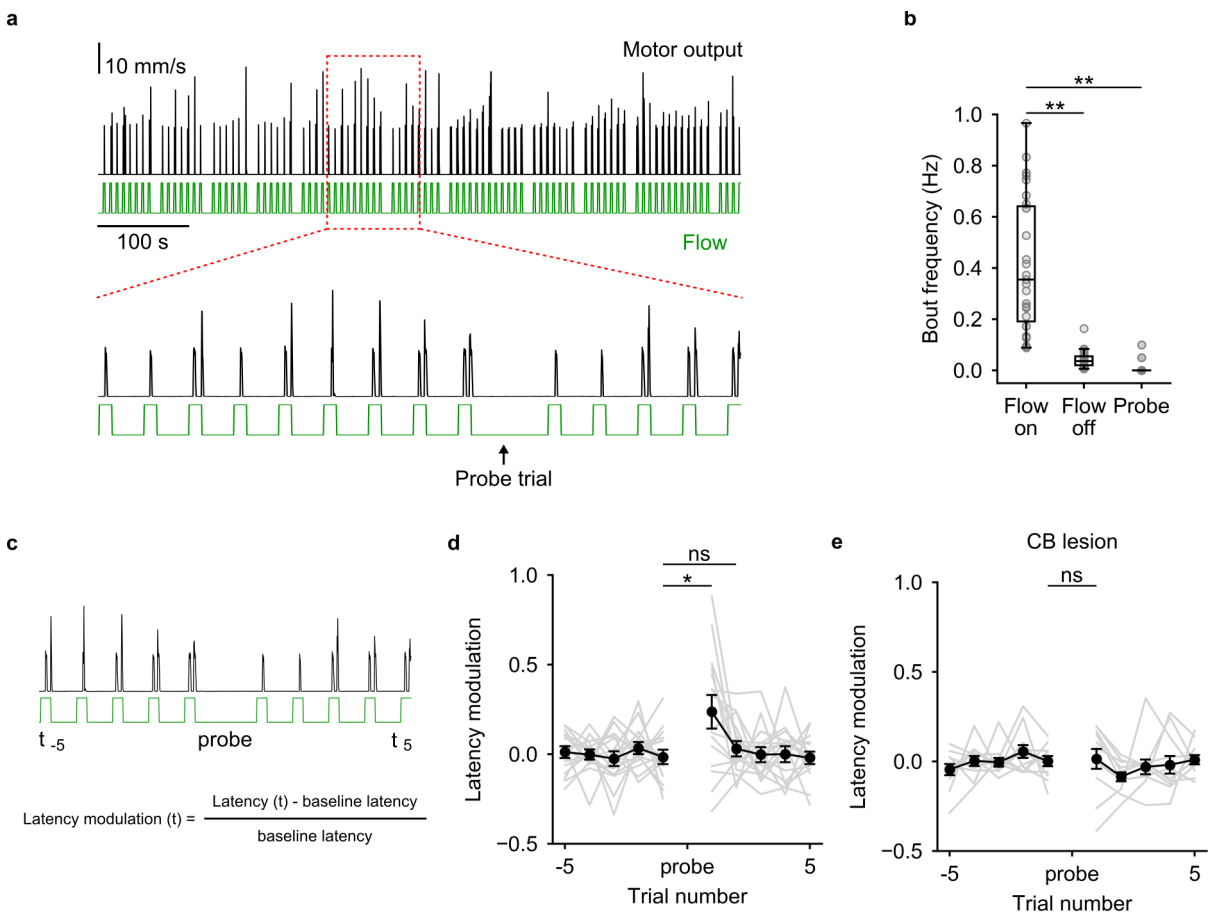

Fig.2: Expectation dependent trial-by-trial modulation of latency.

a, Representative behavior data recorded over one experiment showing discrete swim bouts evoked by optic flow. **b,** Mean bout frequency for each fish over different periods of the experiment. 2s presentation of optic flow reliably evokes swims. Almost no swims were initiated in the optic flow-off period or during probe trials. $p = 1.01 \times 10^{-13}$ by one-way repeated measures ANOVA, 27 fish. **p = 0.001 by Tukey's post hoc test. **c,** Calculating fold change in latency over a baseline for a 10 trial window around a probe trial. The average latency in 5 trials before a probe trial is considered as the baseline latency. **d,** Probe trials induce a transient increase in latency in the next trial. *p = 0.03 by Wilcoxon signed-rank test, 17 fish. Latency returns to baseline after one trial. ns : p = 0.43. **e,** Fish tested after laser ablating the cerebellum did not show an increase in latency in the trial immediately after a probe trial. p = 0.79 by Wilcoxon signed-rank test, 11 fish. Overall behavioral responsiveness remained unaffected (Supplementary Fig. 1).

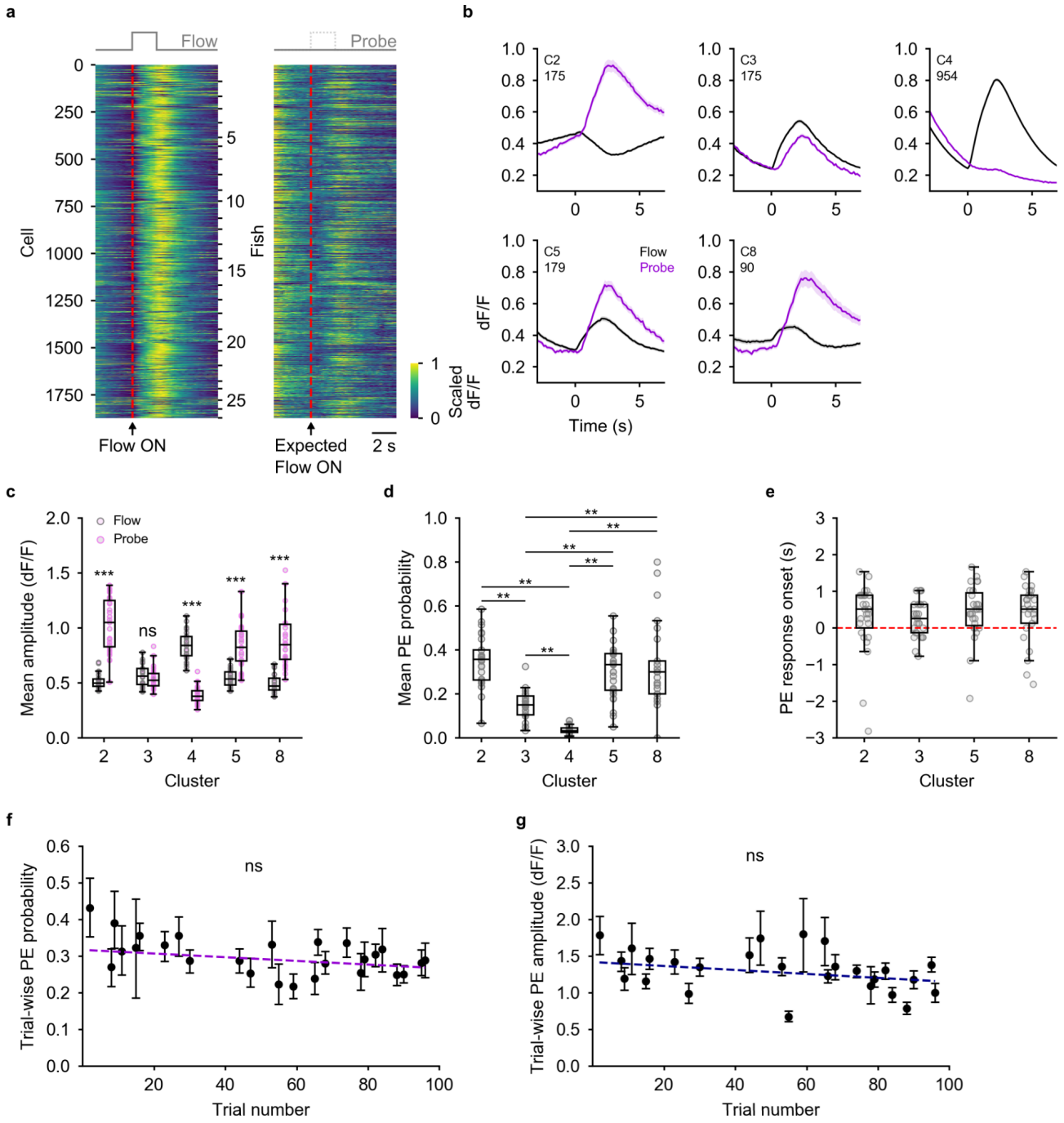

Fig.3: Purkinje cells encode a time-locked prediction error (PE) signal.

a, Optic flow and probe triggered average responses of all 1874 cells recorded from 27 fish. Each cell is normalized to a range of 0 to 1, representing its min and max dF/F. A widespread response to optic flow and to the expected time of onset of optic flow is noticeable across the population.

b, Cells grouped into 5 functional clusters by correlation based hierarchical clustering. Clusters

2, 3, 5 and 8 show large responses tuned to the onset of probe trials and weaker or no response during non-probe trials. Cells in cluster 4 do not show a response during probe trials but show large responses in non-probe trials caused by sensory and/or motor activity. Inset numbers show the number of cells in each cluster. Shaded regions represent SEM across cells in each cluster. **c,** Clusterwise comparison of the amplitude of the probe and flow triggered average responses. Clusters 2, 5 and 8 show significantly larger responses in probe trials. ***$p < 0.001$ by paired t-test, 27 fish. **d,** Average probability of a calcium response occurring in a given cell in a single probe trial. $p = 1.15 \times 10^{-18}$ by one-way ANOVA, 27 fish, **$p < 0.01$ by Tukey's post hoc test. **e,** Time of onset of a calcium response during probe trials relative to the expected onset of optic flow. The probe response is time-locked to the expected onset time of optic flow (statistics in Supplementary Table 1). Dashed red line at t = 0s indicates probe onset. Data points in panels **c-e** represent individual fish. **f,g,** PE response probability and amplitude do not change significantly with trials, p = 0.988 and 0.985 respectively by linear mixed-effects.

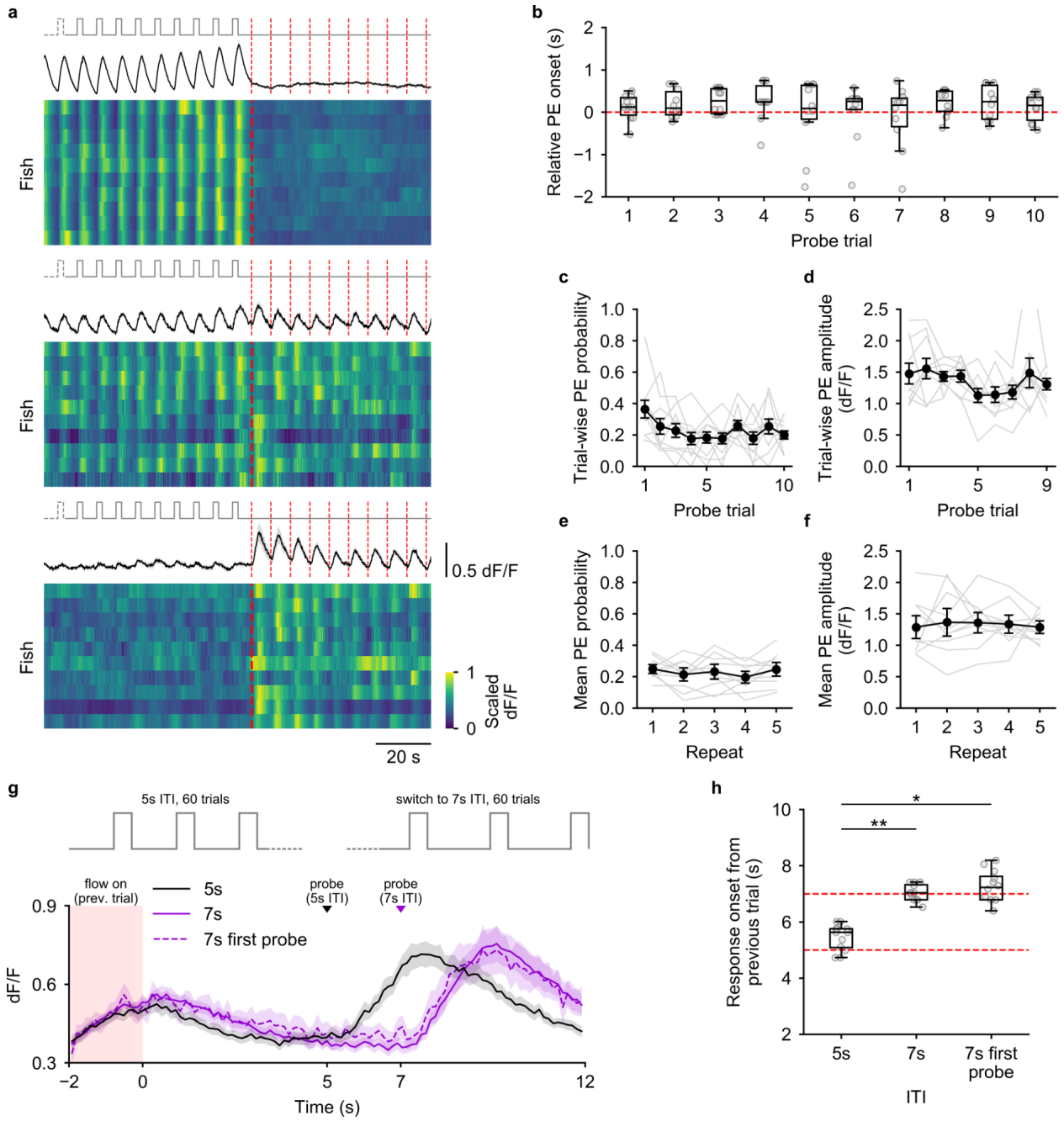

Fig.4: Predictions of optic flow onset are encoded in entrained neuronal activity.

a, Average responses of cells classified as optic flow responsive, entrained, or PE based on correlation with regressors. Shaded regions around calcium traces represent SEM across 10 fish. **b,** Onset times of the PE signal for cells in the bottom panel in **a**, measured relative to the start of a probe trial for each of the 10 consecutive probe trials. Dashed red line indicates probe onset (t = 0s) (statistics in Supplementary Table 2). **c,d,** PE response probability and amplitude for the 10

consecutive probe trials. The PE signal remained robust without optic flow for the full duration of 10 probe trials. **e,f,** No change in PE response probability or amplitude was observed over the 5 repeats of the stimulus protocol. Error bars in **c-f** represent SEM across 10 fish. **g,** Average response of the same cells during probe trials at 5s ITI (black) and 7s ITI (purple). Arrowheads indicate the onset of probe trials for the respective ITIs. Data shown as mean ± SEM. **h,** Onset times of the PE signal measured from the end of the previous trial. $p = 0.006$ by one-way repeated measures ANOVA, $*p = 0.028$, $**p = 0.0067$ by Tukey's post hoc test, 12 fish.

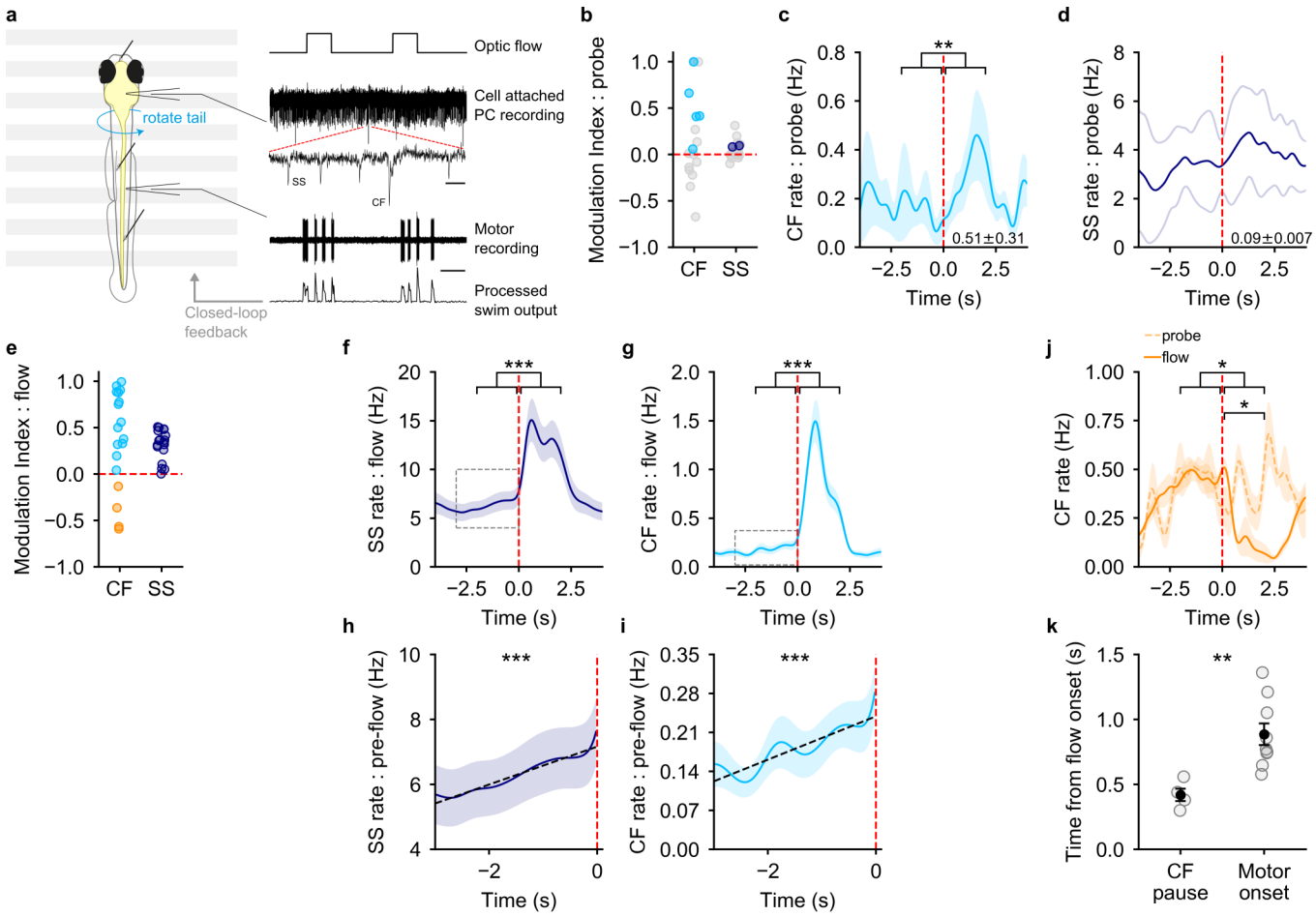

Fig.5: Electrophysiological analysis of predictive responses in Purkinje cells.

a, Experimental preparation showing simultaneously recorded Purkinje cell responses and fictive swim output. Scale, zoomed out : 2s ; zoomed in : 20ms. **b,** CF and SS modulation indices for probe trials for 18 cells. Cells with significant positive modulation (See Methods) are highlighted. **c,** The average CF rate during the probe trials is significantly elevated compared to baseline for the probe responsive cells identified in **b**. **p = 0.0097. **d,** SS responses of the two probe responsive cells identified in **b**, dark line is the average. Average modulation indices are inset in **c,d** as mean ± SD. **e,** CF input and SS optic flow modulation indices for 18 cells. CF input rate is elevated during optic flow in 14 cells (cyan) and suppressed in 4 cells (orange). SS rate is elevated during optic flow compared to pre-flow levels in all cells (purple). **f,** Optic flow triggered SS responses of all cells. ***p = 2 x 10^{-4}. **g,** Optic flow triggered CF responses of cells with positive modulation indices. ***p = 4.8 x 10^{-5}. **h,i,** Pre-trial increase in SS and CF rates in

cells with positive modulation indices (zoom of highlighted pre-trial windows in **f,g**). SS : ***p = 2 x 10^{-4}, CF : ***p = 8.8 x 10^{-6} by linear mixed-effects. Dashed black lines are linear mixed-effects fits. **j,** Optic flow and probe CF responses of cells with negative modulation indices. Pre-probe vs probe : *p = 0.04, probe vs optic flow : *p = 0.039. **k,** CF suppression does not coincide with motor onset. **p = 0.007, t-test. Traces in **c,f-j** show mean ± SEM. p-values in **c,f,g,j** are from paired t-tests. Dashed red lines in **c,d,f-j** indicate the onset of a trial.

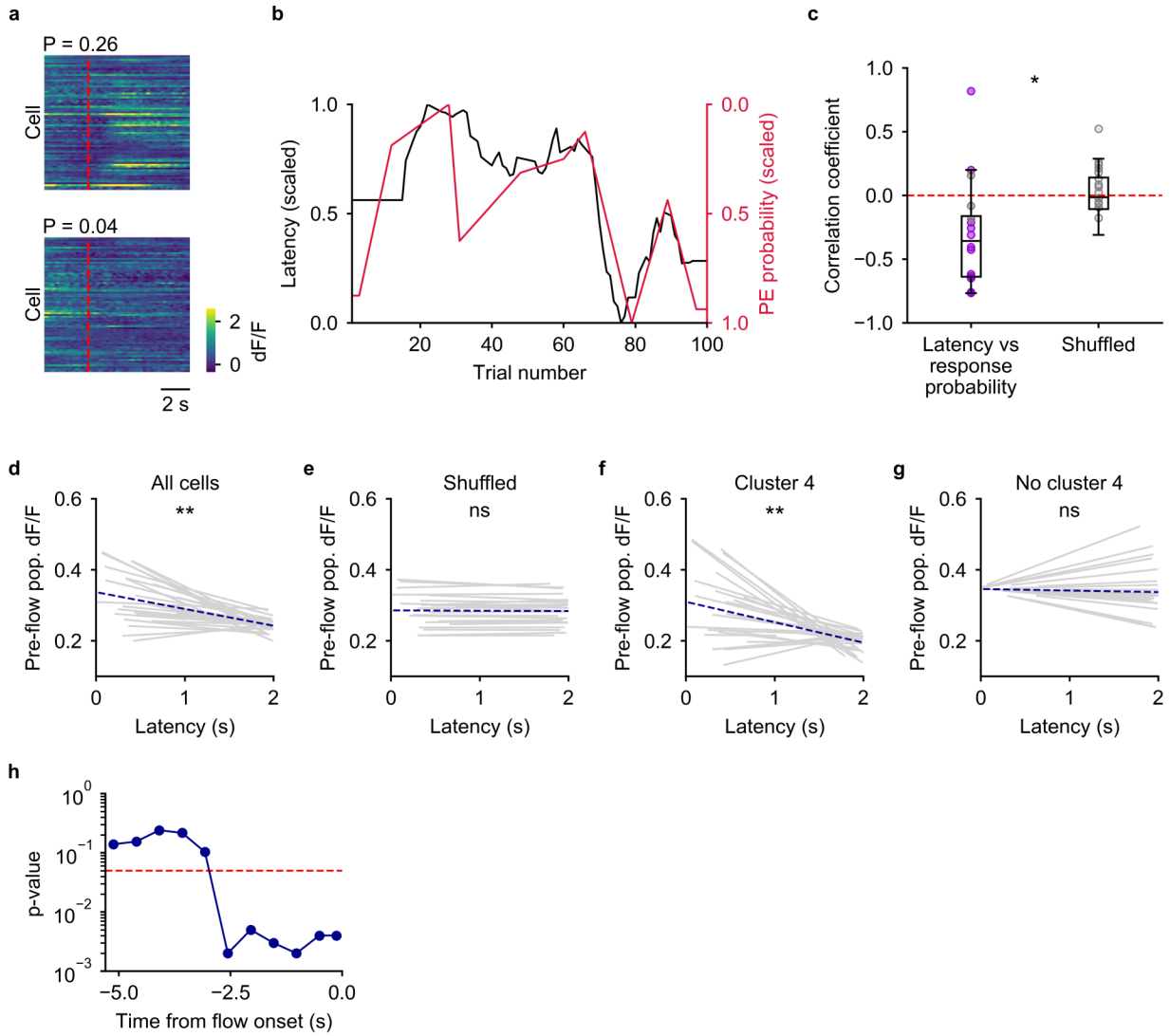

Fig.6: Predictive neural responses are correlated with latency at the single trial level. **a,** Heatmap showing single trial responses of the same cells in two different probe trials with PE response probability 0.26 and 0.04. Dashed red line indicates the start of the probe trial. **b,** Representative plot showing the negative correlation between latency and interpolated PE response probability. **c,** Correlation coefficient between latency and interpolated response probability showing a significant negative correlation when compared to trial shuffled correlation. *p = 0.017 by paired t-test, 16 fish. Data points represent individual fish. Purple markers highlight fish with individually significant correlation ($p < 0.05$, from scipy.stats.pearsonr function) compared to chance. Dashed red line is the mean shuffled correlation. **d-g,** Linear mixed-effects model fits for individual fish (grey lines, N=27) and the

population (dashed blue line) between pre-flow population average dF/F and latency. **d,** A significant negative correlation is present between pre-flow population activity and latency of all cells. **p = 0.001. **e,** No correlation is observed after shuffling the order of trials. p = 0.824. **f,g,** Cells in cluster 4 alone recapture the correlation observed in **d**. **p = 0.004, ns : p = 0.738. **h,** p-values of linear mixed-effects model fits for cluster 4 cells for time points ranging from the first frame prior to the onset of optic flow (same as **f**) to 5s prior to the onset of optic flow. Significant predictive information about latency is present in Purkinje cell activity up to 2.5s prior to trial onset.

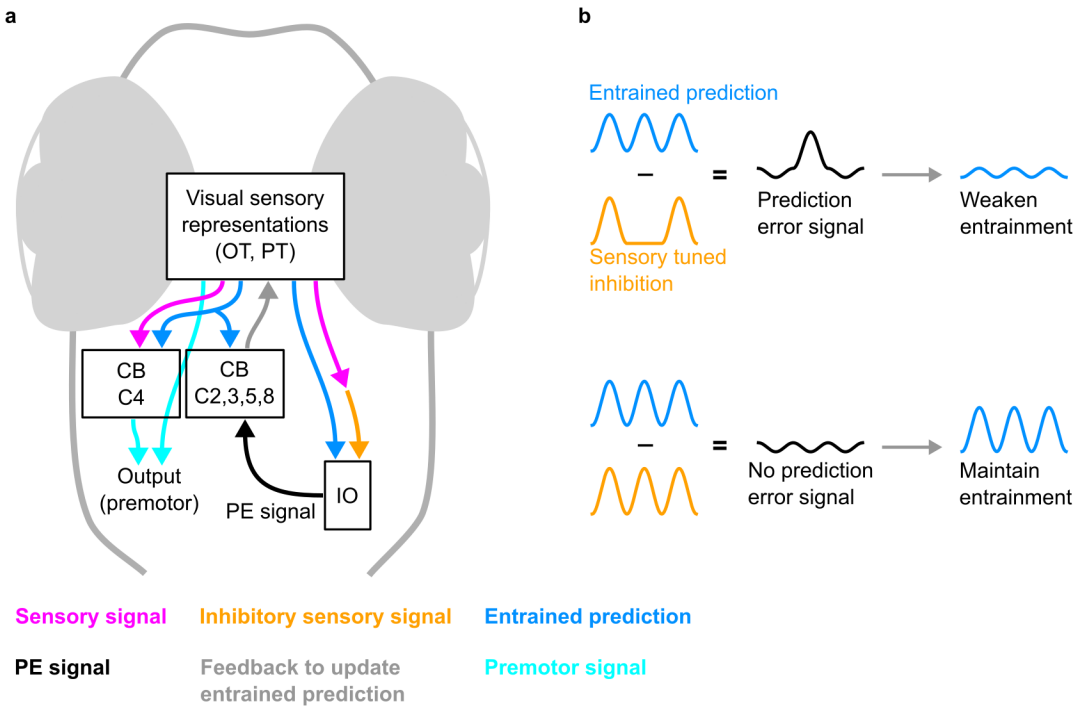

Fig.7: Circuit mechanism for predictive control of behavior.

a, Schematic of circuit model built using previous anatomical and functional data [52–54] and our results. A subcircuit in the cerebellum (C2,3,5 and 8) is involved in acquiring and updating internal representations of the temporal pattern in optic flow in the environment. A second subcircuit (C4) is involved in using these internal representations to predictively plan motor commands. **b,** Schematic showing the proposed mechanism of generation of a PE signal. The PE signal serves to update the entrained internal representation of optic flow when it does not match with sensory input. CB, Cerebellum ; IO, Inferior Olive ; OT, Optic Tectum ; PT, Pretectum.

Supplementary Figures and Tables

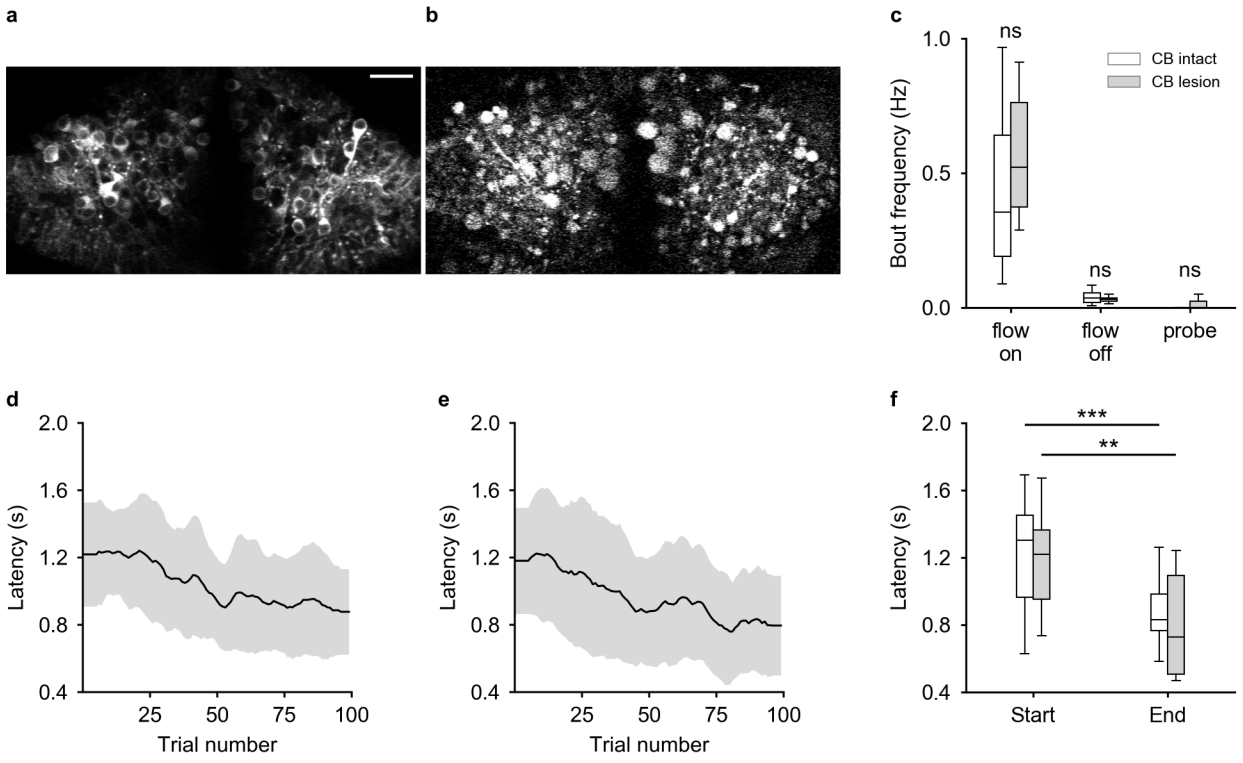

Supplementary Fig.1: Cerebellum lesioned fish show no detectable difference in behavioral responsiveness.

a, A single two-photon optical section of the GCaMP6s expressing Purkinje cells before lesioning. Cell bodies are visible as rings with nuclear exclusion of GCaMP. Scale bar : 20µm. **b,** A single two-photon optical section of the cerebellum in the same fish as shown in **a**, recorded after the ~12 minute long experimental protocol which began 1 hour after lesioning. Disintegration and blebbing of cells and neuropil can be seen. **c,** Bout frequency was unchanged after lesioning. p = 0.11, 0.20 and 0.94 by independent samples t-tests for the optic flow-on, optic flow-off and probe periods respectively, no lesion : 27 fish, lesion : 11 fish. **d,e,** The average latency for **d**, non-lesioned fish and **e**, lesioned fish, over the course of 100 trials. Shaded region represents SD. Latency was interpolated linearly for all 100 trials and a rolling average of 10 trials was calculated for each fish. Fish that did not respond for 10 consecutive trials anywhere during the experiment were excluded. **f,** Comparison of latency at the beginning versus the end of 100 trials. Both lesioned and non-lesioned fish showed a significant drop in latency.

***p = 0.0005, **p=0.003 by paired t-tests, 16 and 11 fish respectively. Latency was not different at the start or the end between lesioned and non-lesioned fish. p = 0.76 and 0.49 by independent samples t-tests, 16 non-lesioned fish and 11 lesioned fish.

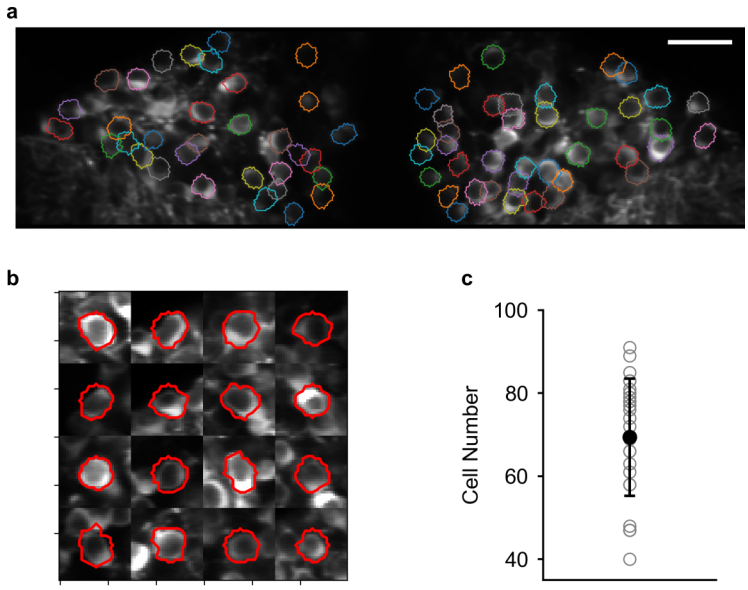

Supplementary Fig.2: Semi-automated identification of cell boundaries.

a, ROIs consisting of Purkinje cell somata marked using a semi-automated neural network based method. Overlapping pixels in neighbouring ROIs are excluded from dF/F calculation to prevent signal contamination. Scale bar : 20µm. **b,** A zoomed-in view of boundaries detected for 16 cells with variable shapes and sizes. **c,** The number of cells obtained from 27 fish. We recorded from 69 ± 14 cells (mean ± SD) per fish.

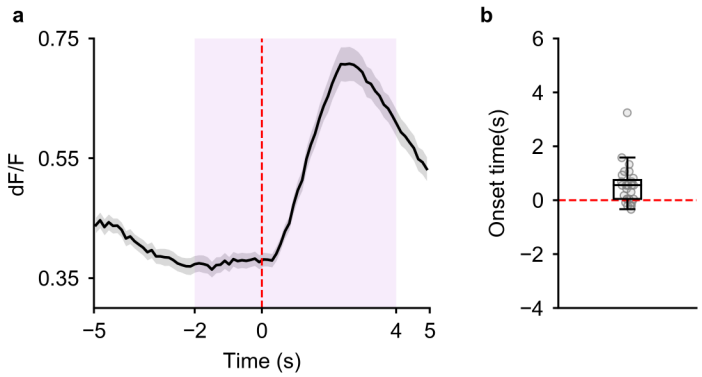

Supplementary Fig.3: Probe responses are specific to the expected onset time of optic flow. **a,** Average response profile of cells picked for showing a significant increase in activity at any time point within the highlighted window -2s to 4s from the onset of a probe trial. Even with the wide window for detection, responses are sharply tuned to the expected onset time of optic flow (t = 0s). Shaded region represents SEM for 27 fish. **b,** Onset times estimated for 27 fish show responses tuned to 0.53 ± 0.73s (mean ± SD). The red dashed line indicates the onset of probe trials.

Cluster	Mean PE onset (s)	SD (s)	p-value
2	0.28	0.94	$<10^{-5}$
3	0.25	0.49	$<10^{-5}$
5	0.44	0.73	$<10^{-5}$
8	0.40	0.78	$<10^{-5}$

Supplementary Table 1: Analysis of time-locking of the response seen in probe trials for clusters 2, 3, 5 and 8.

The table shows mean and standard deviation of the onset time distributions relative to the onset of probe trials for clusters 2, 3, 5 and 8. The window of analysis spanned ±3 seconds from probe onset. The onset time distributions are centered around the onset of probe trials for all the clusters. P-values estimated by a randomization based test (See Methods) show significant time-locking for all clusters compared to what is expected from a uniform distribution in the ±3 window.

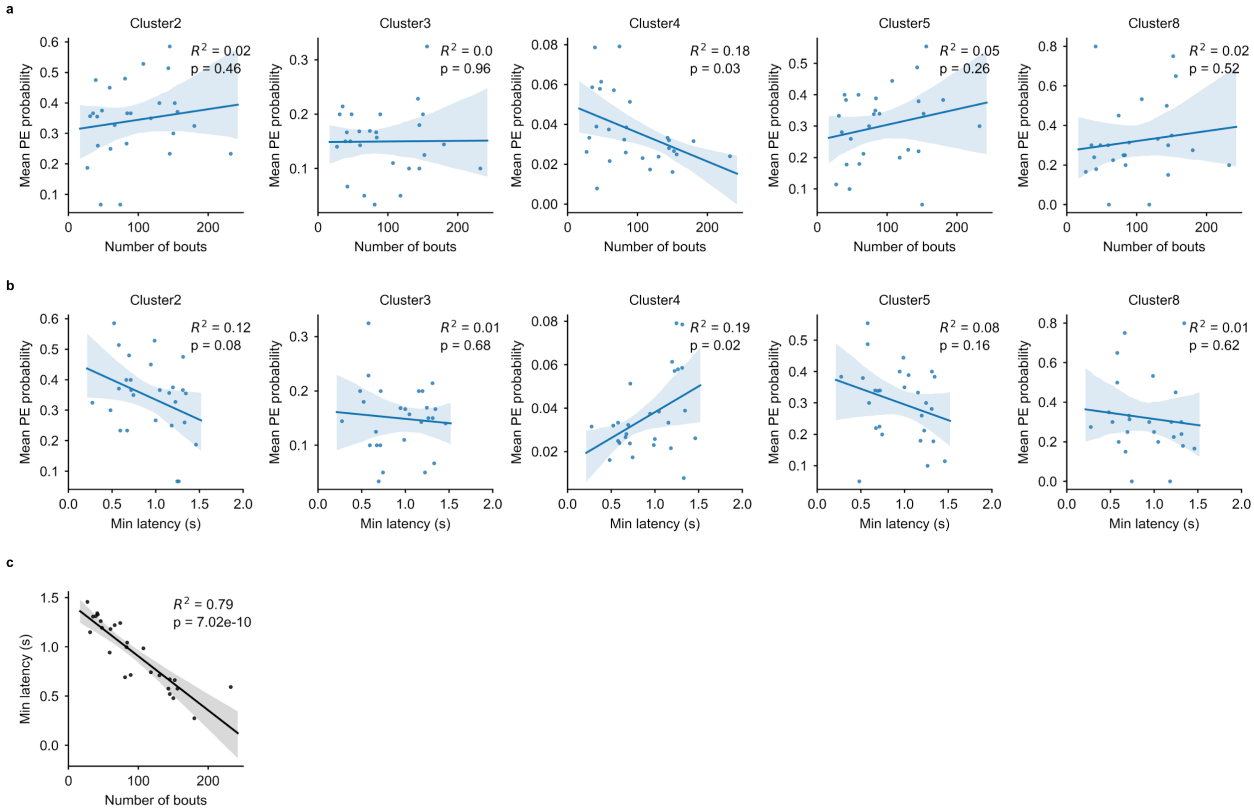

Supplementary Fig.4: PE signals are encoded in Purkinje cells independent of motor output.

a,b, PE response probability is largely independent of the number of swim bouts (**a**) or minimum latency (**b**). Minimum latency is estimated by taking the minimum value of the 10-trial rolling average of latency for each fish. Cluster 4 cells show a weak but significant dependence on average population level indicators of behavioral responsiveness, with lower PE response probability in fish with higher behavioral responsiveness (Cluster 4, **a,b**). **c,** Both number of bouts and minimum latency are strongly correlated to each other and potentially reflect the internal state of each fish. Solid lines show linear regression fits. Shaded regions represent 95% confidence intervals. R^2 for the fits and p-values for Wald test for non-zero slope are inset within each plot. N = 27 fish.

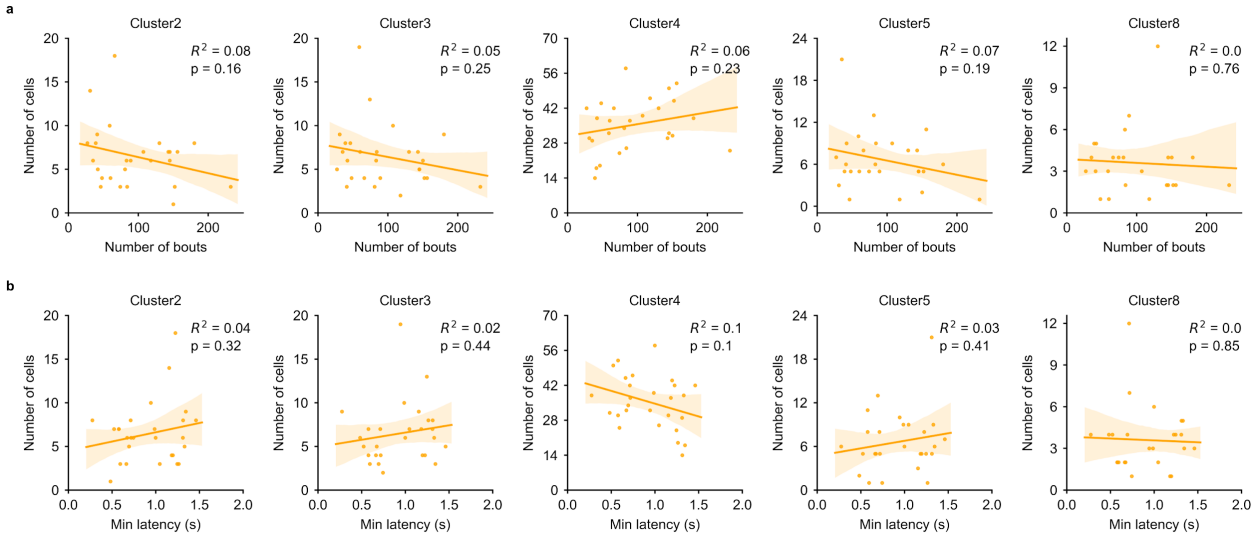

Supplementary Fig.5: Functional distribution of cells is independent of motor output. **a,b,** Distribution of cells across the functional clusters is independent of the number of bouts (**a**) and the minimum latency (**b**). Solid lines show linear regression fits. Shaded regions represent 95% confidence intervals. R^2 for the fits and p-values for Wald test for non-zero slope are inset within each plot. N = 27 fish.

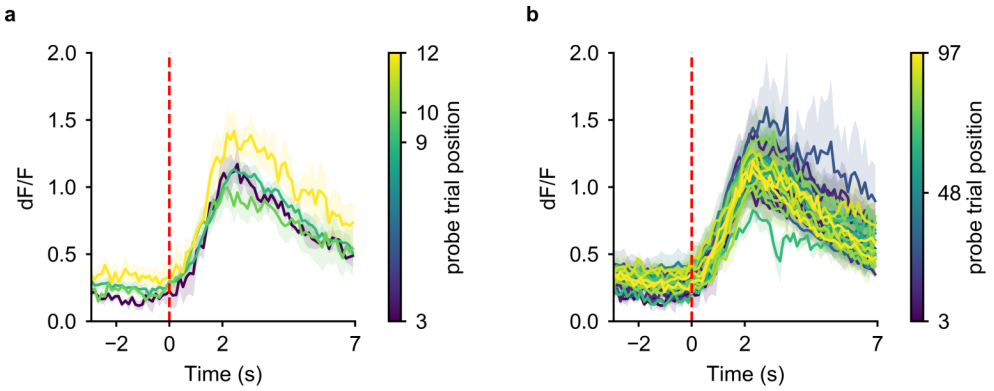

Supplementary Fig.6: Trial-wise probe triggered average responses of cells which show significant increase in activity in each probe trial.

a,b, Trial-wise average PE signal in the first 4 probe trials (**a**) and in all probe trials (**b**). Color scale indicates the position of the probe trial in the experiment. The PE signal in the 3rd trial is indistinguishable from other probe trials later in the experiment. Shaded regions represent SEM across fish.

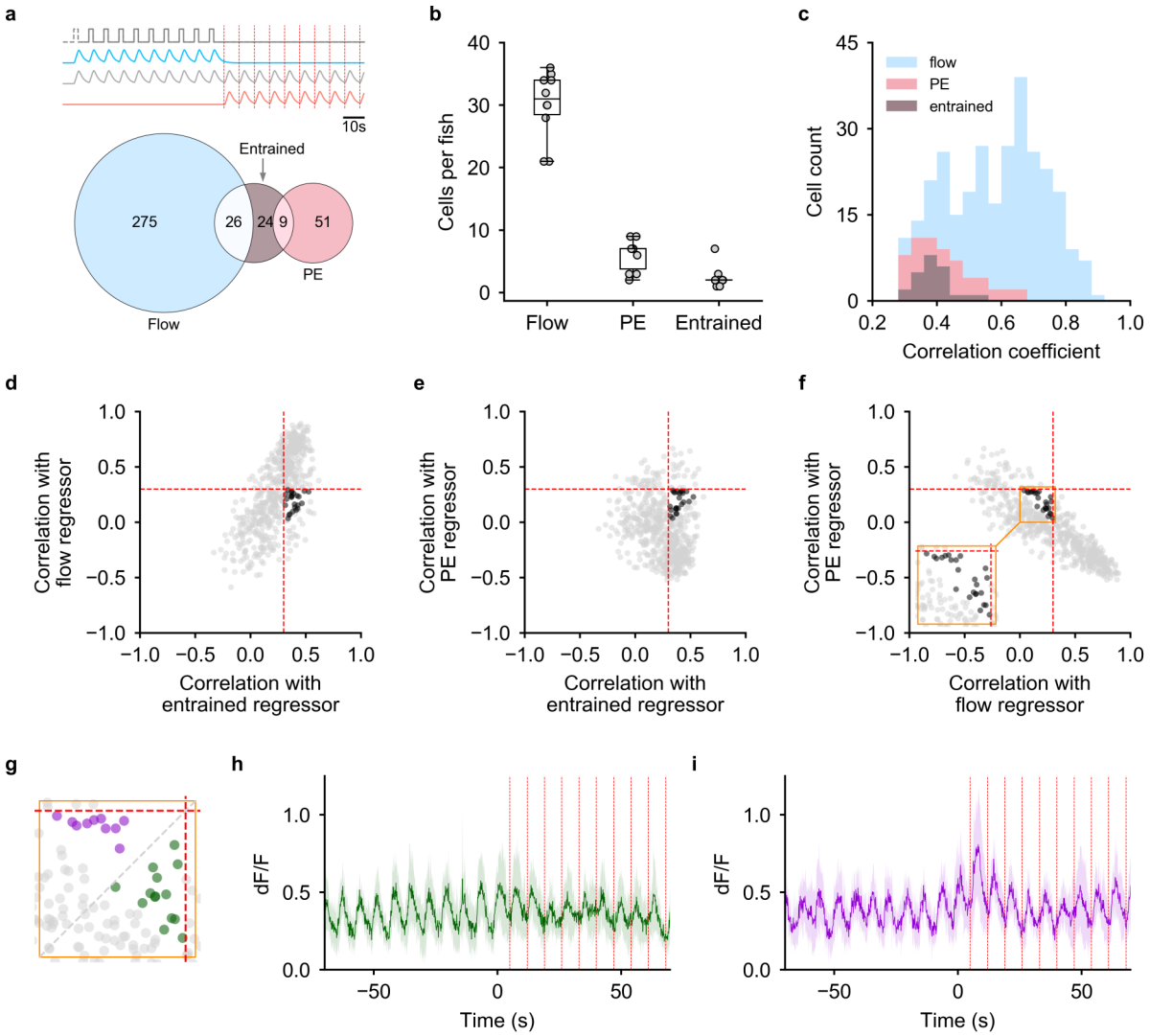

Supplementary Fig.7: Distribution of cells based on correlation with optic flow, entrained and PE regressors.

a, Top: Optic flow, entrained and PE regressors aligned with the optic flow stimulus. Bottom: distribution of cells showing suprathreshold correlation (threshold = 0.3) with optic flow, PE or entrained regressors. **b,** Number of cells per fish classified as optic flow responsive, entrained, or PE. N = 10 fish. **c,** Histogram showing the correlation coefficients of cells in each class. **d-f,** Correlation coefficients of all cells recorded in this experiment across 10 fish. In all cases, the 24 entrained cells are highlighted in black. **g,** A zoomed in window of the region highlighted in **f** with entrained cells that are more optic flow correlated than PE correlated in green and entrained cells that are more PE correlated than optic flow correlated highlighted in purple. Dashed grey

diagonal is the line of equality. **h,i,** Average response of cells highlighted in green and purple respectively in **g**. Shaded regions represent SEM across 8 fish in **h** and 7 fish in **i**. Dashed red lines in **d-g** indicate the threshold correlation of 0.3. Dashed red lines in **a,h,i,** indicate the start time of each consecutive probe trial.

Probe trial	Mean PE onset (s)	SD (s)	p-value
1	0.11	0.29	$<10^{-5}$
2	0.20	0.31	2×10^{-5}
3	0.26	0.28	$<10^{-5}$
4	0.25	0.45	7.7×10^{-4}
5	-0.07	0.82	0.08
6	-0.01	0.64	0.01
7	-0.11	0.72	0.03
8	0.21	0.30	4×10^{-5}
9	0.22	0.38	1.5×10^{-4}
10	0.11	0.32	2×10^{-5}

Supplementary Table 2: Analysis of onset times of the entrained PE responses across 10 consecutive probe trials.

PE responses across 10 consecutive probe trials remain significantly time-locked to the expected onset time of optic flow. The onset times and p-values were estimated within a ±2 second window relative to the start of each probe trial. P-values were estimated using a randomization test described in the methods section and indicate whether there is significant time-locking compared to random sampling from a uniform distribution of onset times spanning the ±2 second window.

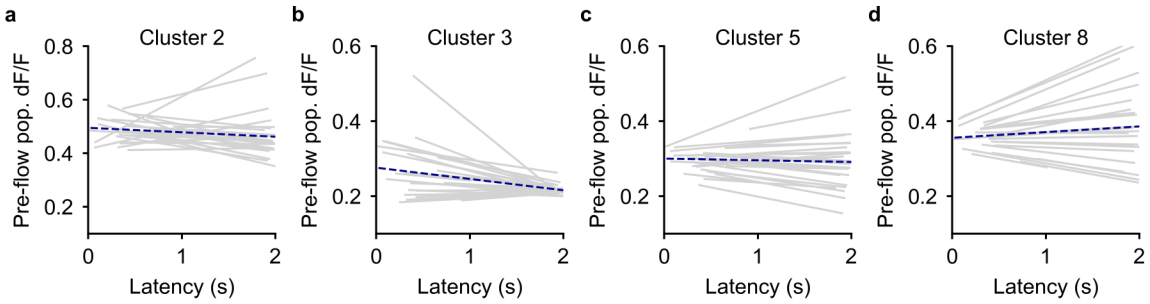

Supplementary Fig.8: Correlation between pre-trial activity and latency for clusters 2, 3, 5 and 8.

a-d, Linear mixed-effects model fits for clusters 2, 3, 5 and 8 show no significant predictive information about latency in these clusters. N of 27 fish, p-values : **a**, 0.492; **b**, 0.069; **c**, 0.819; **d**, 0.544

Supplementary Video 1

Average calcium responses of representative cells from the same fish across 5 trial aligned epochs of the experimental protocol shown in Fig. 1b. Dark blue traces show cells responsive to optic flow and cyan traces highlight cells with strong probe responses. Dashed red line marks probe onset.

Supplementary Video 2

Entrained PE responses in a representative fish. Top panel shows raw fluorescence of Purkinje cells averaged over 5 stimulus blocks. Plots show individual dF/F traces (cyan) and their average (yellow) for the 13 cells indicated by yellow arrowheads in the top panel. Bottom-most trace represents the optic flow stimulus. Purple dashed lines indicate the positions of successive probe trials.

References

1. Fiser, A. *et al.* Experience-dependent spatial expectations in mouse visual cortex. *Nat. Neurosci.* **19**, 1658–1664 (2016).
2. Kennedy, A. *et al.* A temporal basis for predicting the sensory consequences of motor commands in an electric fish. *Nat. Neurosci.* **17**, 416–422 (2014).
3. Kim, S. S., Hermundstad, A. M., Romani, S., Abbott, L. F. & Jayaraman, V. Generation of stable heading representations in diverse visual scenes. *Nature* **576**, 126–131 (2019).
4. Mischiati, M. *et al.* Internal models direct dragonfly interception steering. *Nature* **517**, 333–338 (2015).
5. Wolpert, D. M., Ghahramani, Z. & Jordan, M. I. An internal model for sensorimotor integration. *Science* **269**, 1880–1882 (1995).
6. Zago, M. *et al.* Internal Models of Target Motion: Expected Dynamics Overrides Measured Kinematics in Timing Manual Interceptions. *J. Neurophysiol.* **91**, 1620–1634 (2004).
7. Harvey, C. D., Coen, P. & Tank, D. W. Choice-specific sequences in parietal cortex during a virtual-navigation decision task. *Nature* **484**, 62–68 (2012).
8. Reinhold, A. S., Sanguinetti-Scheck, J. I., Hartmann, K. & Brecht, M. Behavioral and neural correlates of hide-and-seek in rats. *Science* **365**, 1180–1183 (2019).
9. Kawashima, T., Zwart, M. F., Yang, C.-T., Mensh, B. D. & Ahrens, M. B. The Serotonergic System Tracks the Outcomes of Actions to Mediate Short-Term Motor Learning. *Cell* **167**, 933-946.e20 (2016).
10. Leinweber, M., Ward, D. R., Sobczak, J. M., Attinger, A. & Keller, G. B. A Sensorimotor Circuit in Mouse Cortex for Visual Flow Predictions. *Neuron* **95**, 1420-1432.e5 (2017).
11. Angelaki, D. E., Shaikh, A. G., Green, A. M. & Dickman, J. D. Neurons compute internal models of the physical laws of motion. *Nature* **430**, 560–564 (2004).
12. Herzfeld, D. J., Kojima, Y., Soetedjo, R. & Shadmehr, R. Encoding of error and learning to correct that error by the Purkinje cells of the cerebellum. *Nat. Neurosci.* **21**, 736–743 (2018).
13. Narain, D., Remington, E. D., Zeeuw, C. I. D. & Jazayeri, M. A cerebellar mechanism for learning prior distributions of time intervals. *Nat. Commun.* **9**, 469 (2018).
14. Hull, C. Prediction signals in the cerebellum: Beyond supervised motor learning. *eLife* **9**, e54073 (2020).
15. Wolpert, D. M. & Kawato, M. Multiple paired forward and inverse models for motor control.

Neural Netw. **11**, 1317–1329 (1998).

16. Narayanan, S. & Thirumalai, V. Contributions of the cerebellum for predictive and instructional control of movement. *Curr. Opin. Physiol.* **8**, 146–151 (2019).
17. Chabrol, F. P., Blot, A. & Mrsic-Flogel, T. D. Cerebellar Contribution to Preparatory Activity in Motor Neocortex. *Neuron* **103**, 506-519.e4 (2019).
18. Chen, S., Augustine, G. J. & Chadderton, P. The cerebellum linearly encodes whisker position during voluntary movement. *eLife* **5**, e10509 (2016).
19. Giovannucci, A. *et al.* Cerebellar granule cells acquire a widespread predictive feedback signal during motor learning. *Nat. Neurosci.* **20**, 727–734 (2017).
20. Heffley, W. & Hull, C. Classical conditioning drives learned reward prediction signals in climbing fibers across the lateral cerebellum. *eLife* https://elifesciences.org/articles/46764 (2019) doi:10.7554/eLife.46764.
21. Kostadinov, D., Beau, M., Blanco-Pozo, M. & Häusser, M. Predictive and reactive reward signals conveyed by climbing fiber inputs to cerebellar Purkinje cells. *Nat. Neurosci.* **22**, 950–962 (2019).
22. Larry, N., Yarkoni, M., Lixenberg, A. & Joshua, M. Cerebellar climbing fibers encode expected reward size. *eLife* **8**, e46870 (2019).
23. Wagner, M. J., Kim, T. H., Savall, J., Schnitzer, M. J. & Luo, L. Cerebellar granule cells encode the expectation of reward. *Nature* **544**, 96–100 (2017).
24. Gao, Z. *et al.* A cortico-cerebellar loop for motor planning. *Nature* **563**, 113–116 (2018).
25. Kunimatsu, J., Suzuki, T. W., Ohmae, S. & Tanaka, M. Different contributions of preparatory activity in the basal ganglia and cerebellum for self-timing. *eLife* **7**, e35676 (2018).
26. Ohmae, S., Uematsu, A. & Tanaka, M. Temporally Specific Sensory Signals for the Detection of Stimulus Omission in the Primate Deep Cerebellar Nuclei. *J. Neurosci.* **33**, 15432–15441 (2013).
27. Paton, J. J. & Buonomano, D. V. The Neural Basis of Timing: Distributed Mechanisms for Diverse Functions. *Neuron* **98**, 687–705 (2018).
28. Ohmae, S., Kunimatsu, J. & Tanaka, M. Cerebellar Roles in Self-Timing for Sub- and Supra-Second Intervals. *J. Neurosci.* **37**, 3511–3522 (2017).
29. Bell, C. C., Han, V. & Sawtell, N. B. Cerebellum-Like Structures and Their Implications for Cerebellar Function. *Annu. Rev. Neurosci.* **31**, 1–24 (2008).

30. Neuhauss, S. C. F. *et al.* Genetic Disorders of Vision Revealed by a Behavioral Screen of 400 Essential Loci in Zebrafish. *J. Neurosci.* **19**, 8603–8615 (1999).
31. Orger, M. B., Smear, M. C., Anstis, S. M. & Baier, H. Perception of Fourier and non-Fourier motion by larval zebrafish. *Nat. Neurosci.* **3**, 1128–1133 (2000).
32. Portugues, R., Haesemeyer, M., Blum, M. L. & Engert, F. Whole-field visual motion drives swimming in larval zebrafish via a stochastic process. *J. Exp. Biol.* **218**, 1433–1443 (2015).
33. Severi, K. E. *et al.* Neural Control and Modulation of Swimming Speed in the Larval Zebrafish. *Neuron* **83**, 692–707 (2014).
34. Lin, Q. *et al.* Cerebellar Neurodynamics Predict Decision Timing and Outcome on the Single-Trial Level. *Cell* **180**, 536-551.e17 (2020).
35. Knogler, L. D., Kist, A. M. & Portugues, R. Motor context dominates output from purkinje cell functional regions during reflexive visuomotor behaviours. *eLife* **8**, e42138 (2019).
36. Ahrens, M. B. *et al.* Brain-wide neuronal dynamics during motor adaptation in zebrafish. *Nature* **485**, 471–477 (2012).
37. Portugues, R., Feierstein, C. E., Engert, F. & Orger, M. B. Whole-Brain Activity Maps Reveal Stereotyped, Distributed Networks for Visuomotor Behavior. *Neuron* **81**, 1328–1343 (2014).
38. Portugues, R. & Engert, F. Adaptive Locomotor Behavior in Larval Zebrafish. *Front. Syst. Neurosci.* **5**, (2011).
39. Mu, Y. *et al.* Glia Accumulate Evidence that Actions Are Futile and Suppress Unsuccessful Behavior. *Cell* **178**, 27-43.e19 (2019).
40. Markov, D. A., Kist, A. M., Petrucco, L. & Portugues, R. The cerebellum recalibrates a feedback controller involved in motor control. *bioRxiv* 2020.02.12.945956 (2020) doi:10.1101/2020.02.12.945956.
41. Chen, T.-W. *et al.* Ultrasensitive fluorescent proteins for imaging neuronal activity. *Nature* **499**, 295–300 (2013).
42. Hamling, K. R., Tobias, Z. J. C. & Weissman, T. A. Mapping the development of cerebellar Purkinje cells in zebrafish. *Dev. Neurobiol.* **75**, 1174–1188 (2015).
43. Antinucci, P., Folgueira, M. & Bianco, I. H. Pretectal neurons control hunting behaviour. *eLife* **8**, e48114 (2019).
44. Attinger, A., Wang, B. & Keller, G. B. Visuomotor Coupling Shapes the Functional

Development of Mouse Visual Cortex. *Cell* **169**, 1291-1302.e14 (2017).

45. Miri, A., Daie, K., Burdine, R. D., Aksay, E. & Tank, D. W. Regression-Based Identification of Behavior-Encoding Neurons During Large-Scale Optical Imaging of Neural Activity at Cellular Resolution. *J. Neurophysiol.* **105**, 964–980 (2010).
46. Knogler, L. D., Markov, D. A., Dragomir, E. I., Štih, V. & Portugues, R. Sensorimotor Representations in Cerebellar Granule Cells in Larval Zebrafish Are Dense, Spatially Organized, and Non-temporally Patterned. *Curr. Biol.* **27**, 1288–1302 (2017).
47. Kitamura, K. & Häusser, M. Dendritic Calcium Signaling Triggered by Spontaneous and Sensory-Evoked Climbing Fiber Input to Cerebellar Purkinje Cells In Vivo. *J. Neurosci.* **31**, 10847–10858 (2011).
48. Marder, E. & Calabrese, R. L. Principles of rhythmic motor pattern generation. *Physiol. Rev.* **76**, 687–717 (1996).
49. Marder, E. & Thirumalai, V. Cellular, synaptic and network effects of neuromodulation. *Neural Netw.* **15**, 479–493 (2002).
50. Dunn, T. W. *et al.* Brain-wide mapping of neural activity controlling zebrafish exploratory locomotion. *eLife* **5**, e12741 (2016).
51. Wolf, S. *et al.* Sensorimotor computation underlying phototaxis in zebrafish. *Nat. Commun.* **8**, 651 (2017).
52. Kramer, A., Wu, Y., Baier, H. & Kubo, F. Neuronal Architecture of a Visual Center that Processes Optic Flow. *Neuron* **103**, 118-132.e7 (2019).
53. Naumann, E. A. *et al.* From Whole-Brain Data to Functional Circuit Models: The Zebrafish Optomotor Response. *Cell* **167**, 947-960.e20 (2016).
54. Wang, K., Hinz, J., Zhang, Y., Thiele, T. R. & Arrenberg, A. B. Parallel Channels for Motion Feature Extraction in the Pretectum and Tectum of Larval Zebrafish. *Cell Rep.* **30**, 442-453.e6 (2020).
55. Sumbre, G., Muto, A., Baier, H. & Poo, M. Entrained rhythmic activities of neuronal ensembles as perceptual memory of time interval. *Nature* **456**, 102–106 (2008).
56. Heap, L., Goh, C.-C., Kassahn, K. S. & Scott, E. K. Cerebellar Output in Zebrafish: An Analysis of Spatial Patterns and Topography in Eurydendroid Cell Projections. *Front. Neural Circuits* **7**, (2013).
57. Sengupta, M. & Thirumalai, V. AMPA receptor mediated synaptic excitation drives

state-dependent bursting in Purkinje neurons of zebrafish larvae. *eLife* **4**, e09158 (2015).

58. Keller, G. B. & Mrsic-Flogel, T. D. Predictive Processing: A Canonical Cortical Computation. *Neuron* **100**, 424–435 (2018).
59. Harmon, T. C., Magaram, U., McLean, D. L. & Raman, I. M. Distinct responses of Purkinje neurons and roles of simple spikes during associative motor learning in larval zebrafish. *eLife* **6**, e22537 (2017).
60. Ishikawa, T., Shimuta, M. & Häusser, M. Multimodal sensory integration in single cerebellar granule cells in vivo. *eLife* **4**, e12916 (2015).
61. Lopes, G. *et al.* Bonsai: an event-based framework for processing and controlling data streams. *Front. Neuroinformatics* **9**, (2015).
62. Pologruto, T. A., Sabatini, B. L. & Svoboda, K. ScanImage: flexible software for operating laser scanning microscopes. *Biomed. Eng. Online* **2**, 13 (2003).
63. Walt, S. van der *et al.* scikit-image: image processing in Python. *PeerJ* **2**, e453 (2014).
64. Virtanen, P. *et al.* SciPy 1.0: fundamental algorithms for scientific computing in Python. *Nat. Methods* **17**, 261–272 (2020).
65. Seabold, S. & Perktold, J. Statsmodels: Econometric and Statistical Modeling with Python. in 92–96 (2010). doi:10.25080/Majora-92bf1922-011.